Bioactive Materials 33 (2024) 483–496

Contents lists available at ScienceDirect

Bioactive Materials

journal homepage: www.keaipublishing.com/en/journals/bioactive-materials

Ca & Mn dual-ion hybrid nanostimulator boosting anti-tumor immunity *via* ferroptosis and innate immunity awakening

Xi Deng [a,b], Tianzhi Liu [a,**], Yutong Zhu [a,b], Jufeng Chen [a,b], Ze Song [a,b], Zhangpeng Shi [a,d], Hangrong Chen [a,b,c,d,*]

[a] State Key Laboratory of High Performance Ceramics and Superfine Microstructure, Shanghai Institute of Ceramics, Chinese Academy of Sciences, Shanghai, 200050, PR China
[b] Center of Materials Science and Optoelectronics Engineering, University of Chinese Academy of Sciences, Beijing, 100049, PR China
[c] School of Chemistry and Materials Science, Hangzhou Institute for Advanced Study, University of Chinese Academy of Sciences, Hangzhou, 310024, PR China
[d] Nanotechnology and Intestinal Microecology Research Center, Shanghai Tenth People's Hospital, School of Medicine, Tongji University, Shanghai, 200072, PR China

ARTICLE INFO

Keywords:
Immunotherapy
Ferroptosis
Innate immunity
STING signaling pathway
Calcium carbonate nanoparticles
Manganese

ABSTRACT

Limited by low tumor immunogenicity and the immunosuppressive tumor microenvironment (TME), triple-negative breast cancer (TNBC) has been poorly responsive to immunotherapy so far. Herein, a Ca & Mn dual-ion hybrid nanostimulator (CMS) is constructed to enhance anti-tumor immunity through ferroptosis inducing and innate immunity awakening, which can serve as a ferroptosis inducer and immunoadjuvant for TNBC concurrently. On one hand, glutathione (GSH) depletion and reactive oxygen species (ROS) generation can be achieved due to the mixed valence state of Mn in CMS. On the other hand, as an exotic Ca^{2+} supplier, CMS causes mitochondrial Ca^{2+} overload, which further amplifies the oxidative stress. Significantly, tumor cells undergo ferroptosis because of the inactivation of glutathione peroxidase 4 (GPX4) and accumulation of lipid peroxidation (LPO). More impressively, CMS can act as an immunoadjuvant to awaken innate immunity by alleviating intra-tumor hypoxia and Mn^{2+}-induced activation of the STING signaling pathway, which promotes polarization of tumor-associated macrophages (TAMs) and activation of dendritic cells (DCs) for antigen presentation and subsequent infiltration of tumor-specific cytotoxic T lymphocytes (CTLs) into tumor tissues. Taken together, this work demonstrates a novel strategy of simultaneously inducing ferroptosis and awakening innate immunity, offering a new perspective for effective tumor immunotherapy of TNBC.

1. Introduction

Breast cancer is the most common malignancy worldwide, of which triple-negative breast cancer (TNBC) is a recalcitrant type [1,2]. The longstanding lack of effective therapies results in the poor outcomes of TNBC [3]. In recent decades, cancer immunotherapy, as an exciting type of treatment that stimulates the immune system to fight cancer, has become a clinically validated treatment for many cancers [4]. However, TNBC as an inherent immune cold tumor, has been weak responsive to immunotherapy so far [5,6]. On one hand, during tumor development and progression, TNBC cells evade the host immune system by reducing their immunogenicity, becoming resistant to conventional therapy, and failing to effectively induce immunogenic death, thereby limiting the production and intratumoral infiltration of tumor-specific cytotoxic T lymphocytes (CTLs) [7]. On the other hand, the immunosuppressive tumor microenvironment (TME) of TNBC differs from other subtypes in that there are a large number of tumor-infiltrating immune cells which may hinder the activation of innate immune cells and contribute to tumor progression by regulating proliferation, angiogenesis and immune suppression [8–10]. Thus, the dual immunomodulatory strategy of effectively inducing tumor cell immunogenic death and reversing immunosuppressive TME provides a new treatment option for TNBC patients.

New types of programmed cell death, *e.g.,* ferroptosis, have drawn

Peer review under responsibility of KeAi Communications Co., Ltd.
* Corresponding author. State Key Laboratory of High Performance Ceramics and Superfine Microstructure, Shanghai Institute of Ceramics, Chinese Academy of Sciences, Shanghai, 200050, PR China.
** Corresponding author.
E-mail addresses: liutianzhi@mail.sic.ac.cn (T. Liu), hrchen@mail.sic.ac.cn (H. Chen).

https://doi.org/10.1016/j.bioactmat.2023.11.017
Received 18 September 2023; Received in revised form 8 November 2023; Accepted 24 November 2023

massive attention in developing new cancer therapies ever since their identification, especially for those that are resistance to conventional therapies like TNBC [11,12]. Mechanistically, ferroptosis is mainly controlled by the glutathione (GSH) redox system [13]. Depletion of GSH leads to the inactivation of glutathione peroxidase 4 (GPX4) with the excessive production of cytotoxic reactive oxygen species (ROS), resulting in the accumulation of lipid peroxidation (LPO) and subsequent ferroptosis [14]. TNBC is particularly vulnerable to ferroptosis inducers. For instance, Li et al. constructed a nanoreactor (Au/Cu-TCPP (Fe)@RSL3-PEG-iRGD nanosheet) for ferroptosis activation in TNBC, achieving effective tumor growth inhibition [15]. Cheng et al. prepared an iridium single-atom nanocatalyst (Pt@IrSAC/RBC) to boost ferroptosis therapy, demonstrating superior therapeutic efficacy in a murine TNBC model [16]. Interestingly, it is found that the dying ferroptotic cancer cells are immunogenic as the affected cells could release tumor-associated antigens (TAAs), damage-associated molecular patterns and alarmins, which promote immune activation [17–20]. Currently, ferroptosis inducers are primarily iron-based nanomaterials to directly increase intracellular ferrum (Fe) concentration to promote ROS generation, and ferroptosis-inducing small molecule drugs (*e.g.*, erastin and RSL3) to interfere with the antioxidant systems (such as GPX4) [21,22]. Besides, a non-ferrous ferroptosis-like strategy has also been developed by integrating synergistic ROS burst and GSH depletion into one nanoplatform [23,24]. Transition metals, especially manganese (Mn)-based nanomaterials, exhibit a satisfactory ability to disrupt redox homeostasis, which shows great potential for ferroptosis induction [25,26]. Moreover, unlike the metal-based Fenton or Fenton-like reaction, Ca^{2+} overload in cancer cells is found to increase intracellular ROS levels by destroying mitochondria [27–29]. What is more noting is that a prolonged imbalance of oxidative stress alters the function of proteins, leading to the desensitization of calcium-related channels and uncontrollable accumulation of cellular Ca^{2+} [30].

For TNBC, the process of immune activation is also severely restricted by the immunosuppressive TME [9,10,31,32]. As key innate immune cells, dendritic cells (DCs) have the most robust antigen-presenting function, and play irreplaceable roles in human innate immunity and adaptive immunity [33]. However, the function of DCs is inhibited by the immunosuppressive TME, resulting in blocked activation of the antitumor immune response. Impressively, the stimulator of interferon genes (STING) pathway has emerged as a critical innate immune pathway for relieving the immunosuppressive TME by stimulating the secretion of type-I interferon (IFN-I) and other pro-inflammatory cytokines, which can enhance the function of immune cells [34–36]. Apart from inducing ferroptosis, Mn^{2+} provides a commendable opportunity to enhance the sensitivity of the STING pathway, which favors the activation of innate immune cells and the initiation of a highly efficient anti-tumor immune response [37–40]. In addition, the recruitment and infiltration of anti-inflammatory M2-type tumor-associated macrophages (TAMs) at the tumor tissue are also the major culprits leading to the low anti-tumor immune response [41–43]. Very recently, our group developed an O_2 self-supplying strategy to promote TAMs polarization from M2 to M1 phenotype and reshape the immunosuppressive TME for the effective inhibition of TNBC tumor growth [44,45]. Thus, it is believed that alleviating tumor hypoxia is an effective strategy to promote the polarization of TAMs from M2 to M1 phenotype and awaken the innate immune system, thereby promoting the anti-tumor immune response [44,46–48].

Based on the above considerations, herein, a Ca & Mn dual-ion hybrid nanostimulator (CMS) was constructed to serve as a ferroptosis inducer and immunoadjuvant for TNBC concurrently. Specifically, as shown in Scheme 1, CMS can achieve simultaneous GSH depletion and ROS generation in tumor cells due to the mixed valence state of Mn in CMS. Besides, CMS as an exotic Ca^{2+} provider boosts intracellular Ca^{2+} level, leading to mitochondrial Ca^{2+} overload, which further amplifies the oxidative stress. Deeper, the synergy of GSH depletion and ROS burst of CMS further leads to the accumulation of LPO and subsequent ferroptosis in tumor cells, as well as the release of TAAs and anti-tumor immune activation. Moreover, CMS can alleviate intra-tumor hypoxia and awaken the innate immune system by catalyzing the decomposition of H_2O_2 to produce O_2, which further decreases the expression of HIF-1α and promotes the TAMs polarization from M2 to M1 phenotype. More impressively, Mn^{2+}-induced activation of the STING signaling pathway promotes the secretion of IFN-I and pro-inflammatory cytokines, which is beneficial for efficient activation of DCs for antigen presentation and subsequent infiltration of CTLs into tumor tissue. In brief, such a novel constructed Ca & Mn dual-ion hybrid nanostimulator is endowed with ferroptosis inducing by synergetic GSH depletion, ROS burst and Ca^{2+} overload, as well as innate immunity awakening by alleviating intra-tumor hypoxia and activating the STING signaling pathway, thereby significantly relieving the immunosuppressive TME and enhancing anti-tumor immunity, which offers a new perspective for effective tumor immunotherapy of TNBC.

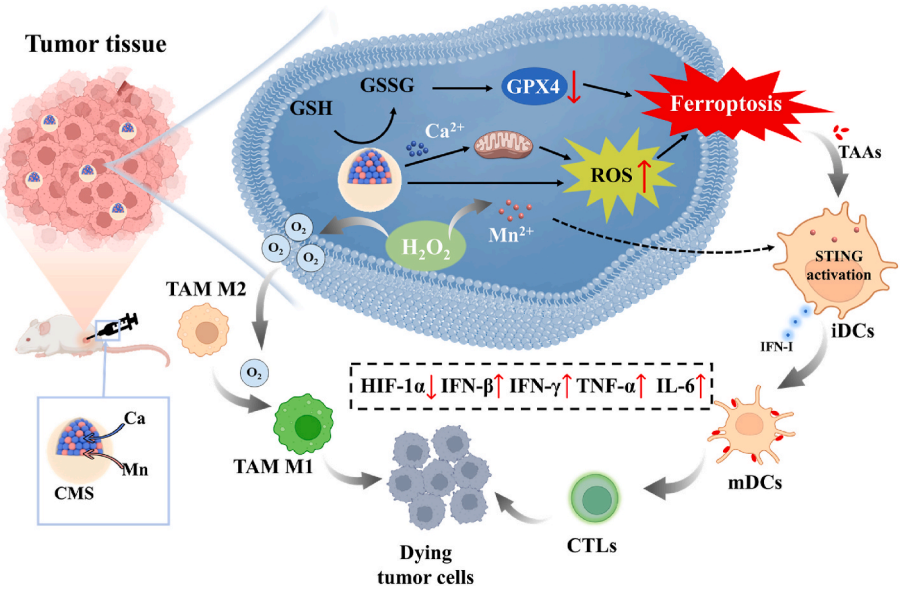

Scheme 1. Schematic illustration of the nanostimulator (CMS) inducing ferroptosis of tumor cells meanwhile awakening TAMs and DCs to boost anti-tumor immune response.

2. Results and discussion

2.1. Synthesis and characterization of CMS

The synthesis of CMS is based on our previous report [49], and the synthesis procedure is shown in Fig. 1a. First, the $CaCO_3$ nanoparticles were synthesized by the gas diffusion reaction. The transmission electron microscopy (TEM) image shows that the $CaCO_3$ has a uniform spherical shape with a diameter of around 150 nm (Fig. S1). Next, CM nanoparticles with a diameter of around 120 nm were prepared by cation exchange of $CaCO_3$ with Mn^{2+} (Fig. S2). Finally, silica was integrated to this system to obtain CMS nanoparticles, which have a diameter of approximately 130 nm with a uniform spherical topography and rough surface (Fig. 1b and Figs. S3 and 4). The dark-field scanning TEM (STEM) image and its corresponding energy-dispersive X-ray spectroscopy (EDS) element mapping and element line scanning indicate the uniform distribution of Ca, Mn, Si and O in the CMS nanoparticles (Fig. 1c). The molar ratio of Mn and Ca in the CMS sample was determined to be approximately 1:1.86 by inductively coupled plasma-optical emission spectrometry (ICP-OES) (Table S1). Notably, CMS showed acid-responsive release behavior for Ca and Mn, mainly due to the acid-responsive performance of carbonate (Fig. S5). The release of Mn was lower than that of Ca, possibly due to a stronger interaction between Mn and the material matrix (much lower solubility product constant (K_{sp}) value of $MnCO_3$ ($K^{\theta}_{sp}(MnCO_3) = 2.3 \times 10^{-11}$), as compared to $CaCO_3$ ($K^{\theta}_{sp}(CaCO_3) = 2.8 \times 10^{-9}$)). Moreover, as shown in Fig. S6, obvious morphology change of CMS was observed after immersing CMS in PBS buffer at pH 5.5, implying the acid-responsive gradual decomposition occur in CMS. The dynamic light scattering (DLS) profiles show that the hydrodynamic size of $CaCO_3$, CM and CMS were 200, 187 and 211 nm, respectively, all with a narrow size distribution (PDI <0.02) (Fig. 1d). Besides, the surface zeta potentials of the nanoparticles changed from +8.5 to −14.9 mV after silica incorporation (Fig. 1e), and the obtained CMS showed better dispersibility in saline (Fig. S7), indicating that the successful integration of silica is much beneficial to improve the stability. The prepared CMS demonstrated an excellent stability in both water and serum (Fig. S8). Moreover, no hemolysis (less than 1.44 %) was observed in red blood cells incubated with the CMS (Fig. S9), laying the foundation for possible biomedical applications of CMS. In addition, the Fourier transform infrared (FTIR) spectrum further confirms the coexistence of carbonated component (CO_3^{2-}) and silica framework (Si–O–Si and Si–O) in CMS (Fig. 1f). The X-ray diffraction (XRD) patterns show the amorphous structure of NPs (Fig. S10). All the above results confirmed the successful synthesis of CMS.

The X-ray photoelectron spectroscopy (XPS) survey spectrum indicates that CMS is composed of Mn, O, Ca, C and Si (Fig. S11a). Moreover, the Ca 2p exhibits two main fitting peaks at 347.3 eV (Ca $2p_{3/2}$) and 350.9 eV (Ca $2p_{1/2}$), which are ascribed to Ca^{2+} (Fig. S11b). Besides, as shown in Fig. S11c, the Mn 2p shows two main fitting peaks at 642.4 eV (Mn $2p_{3/2}$) and 653.9 eV (Mn $2p_{1/2}$). But it is difficult to accurately analyze the valence of Mn, since the peak positions of Mn 2p in the various chemical state of Mn are extremely approximate. Thus, the Mn 3s spectrum was conducted for further information [25].

The average oxidation state (AOS) of Mn can be calculated from the

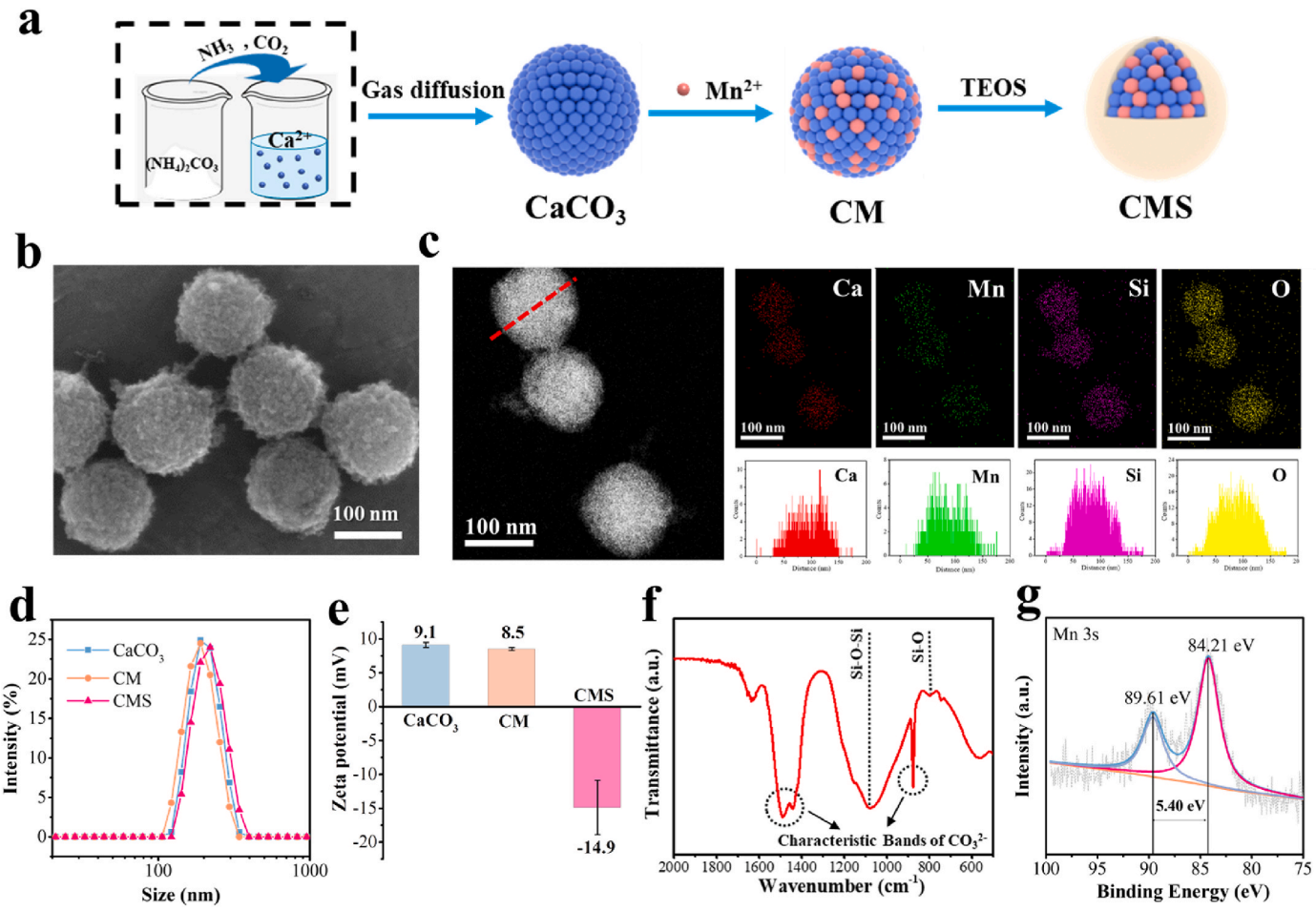

Fig. 1. Synthesis and characterizations of CMS. a) Schematic illustration of the synthesis procedure of CMS. b) SEM image of CMS. c) Dark-field STEM image of CMS and its corresponding EDS element mapping and element line scanning. d) Dynamic light scattering (DLS) results and e) ζ-potentials of $CaCO_3$, CM and CMS. f) FTIR spectrum of CMS. g) High-resolution XPS spectrum of Mn 3s of CMS.

energy separation (ΔEs) in the Mn 3s multiplet splitting according to the following relationship [50]:

$$AOS = 8.95 - 1.13\Delta Es\ (eV)$$

Energy separation of 5.40 eV was obtained for CMS (Fig. 1g), resulting in an AOS of 2.85, which indicates the mixed valence state of Mn. And this mixed valence state of Mn may endow CMS a variety of catalytic properties.

2.2. GSH depletion, O_2 production and ROS generation properties of CMS

GSH is a significant importance and a large amount of antioxidant in tumor cells, which maintains the redox balance and protects tumor cells from damage caused by ROS, thereby promoting tumor growth [51]. Thus, the GSH depletion capacity of CMS was then studied. Ellman's reagent [5,5′-dithiobis (2-nitrobenzoic acid), DTNB] was chosen as an indicator based on its specificity to recognize sulfhydryl groups at 412 nm of UV–vis absorbance peak. As shown in Fig. 2a, 73.4 % of GSH was consumed by CMS (200 μg/mL) within 4 h, in comparison with 95.4 % of GSH depleted by H_2O_2 (3 mM) as a positive control group. Furthermore, the consumption of GSH by CMS increased significantly with increasing incubation time, and 88.9 % of GSH was depleted after 12 h, indicating excellent GSH-depleting ability of CMS ascribed to the presence of high-valent Mn in the CMS (Fig. 2b and Fig. S12).

Afterward, the O_2 generation capability of CMS was evaluated. As shown in Fig. 2c, the mixture of CMS with H_2O_2 solution resulted in a significant increase in dissolved O_2 concentration, implying the large amount of O_2 generation. By contrast, no obvious O_2 production was detected in either the CMS alone group or the H_2O_2 alone group. Moreover, the rate and amount of O_2 production is found to be positively correlated with H_2O_2 concentrations (Fig. 2d), which is attributed to the fact that CMS can catalyze the decomposition of H_2O_2 to produce O_2. This O_2 generation capability endows CMS great potential to alleviate hypoxia in the tumor region.

Besides, the ROS generation capability of CMS was further verified using a colorimetric method based on the decolorization of methylene blue (MB) after selective ·OH trapping. Bicarbonate (HCO_3^-) species functions as a ligand to chelate metal ions, resulting in the rate acceleration of the reaction with H_2O_2, which is indispensable for the Mn^{2+}-mediated Fenton-like reaction according to most of the literature [52–55]. Thus, the test of UV–vis absorption spectra of MB in $NaHCO_3$ buffer under different treatments was conducted, as shown in Fig. 2e. It is clearly found that significant decrease in MB absorbance is detected in the CMS + H_2O_2 group, while negligible changes in MB absorbance are found in the blank, H_2O_2 alone and CMS alone groups. The kinetic curves of MB degradation in Fig. 2f further show the degradation of MB over time. In particular, the degradation rate of MB in the CMS + H_2O_2 group reaches as high as 85.0 % after 30 min, indicating that CMS can effectively catalyze H_2O_2 to produce ROS. Moreover, the generation of ROS was further verified by electron spin resonance (ESR) spectroscopy using 5,5-dimethyl-1-pyrroline N-oxide (DMPO) as a spin trapping agent. The CMS + H_2O_2 group shows distinct ESR signal with an intensity ratio of 1: 2: 2: 1 confirming the production of ·OH radicals (Fig. 2g). These experimental results demonstrated that CMS can effectively induce the decomposition of H_2O_2 to produce ·OH via the Mn (II)-catalyzed Fenton-like reaction.

Taken together, the obtained CMS not only has the ability to deplete GSH, but also has the potential to decompose H_2O_2 and exhibit excellent catalytic activities to simultaneously generate O_2 and ·OH, showing great promise for antitumor application (Fig. 2h).

2.3. In vitro therapeutic efficiency and underlying mechanism of CMS

Encouraged by the results mentioned above, we then investigated the performance of CMS at the cellular level to further evaluate therapeutic outcomes against tumor cells. First, the effect of the materials on

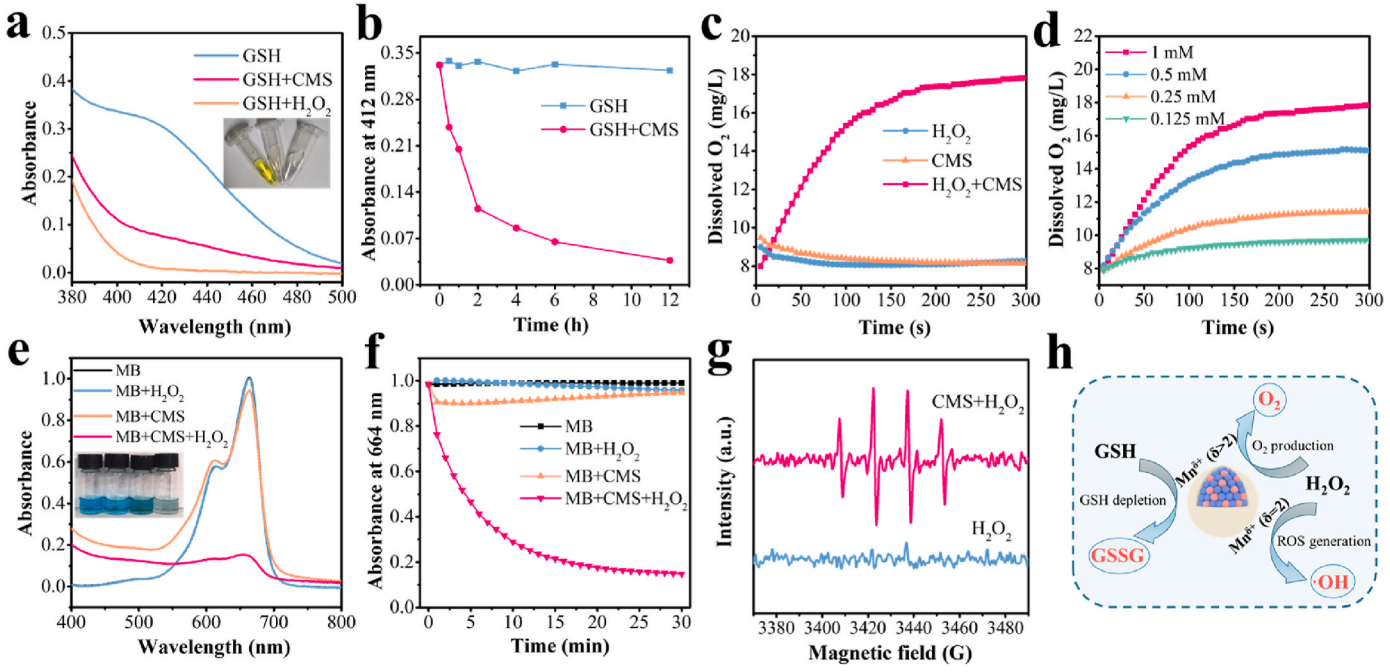

Fig. 2. GSH depletion, O_2 production and ROS generation assay. a) UV–vis absorption spectra of DTNB treated with GSH alone, GSH + CMS and GSH + H_2O_2, respectively. Inset: the digital photograph of the corresponding solution. b) The corresponding absorbance at 412 nm vs time for two different treatments (GSH and GSH + CMS). c) Dissolved O_2 concentration vs time in solutions with H_2O_2, CMS and CMS + H_2O_2, respectively. d) Dissolved O_2 concentration vs time in solution with CMS + H_2O_2 at varied H_2O_2 concentrations. e) UV–vis absorption spectra of MB in $NaHCO_3$ buffer under different treatments (Blank, H_2O_2, CMS and CMS + H_2O_2). Inset: the digital photograph of the corresponding solution. f) The corresponding absorbance at 664 nm vs time for different treatments (Blank, H_2O_2, CMS and CMS + H_2O_2). g) ESR spectra of H_2O_2 and CMS + H_2O_2 using DMPO as the ·OH trapping agent. h) Schematic diagram of GSH depletion and catalytic H_2O_2 decomposition feature of CMS with multi-valent Mn.

the viability of 4T1 tumor cells was evaluated using the standard Cell Counting Kit-8 (CCK8) assay. As shown in Fig. 3a, the Mn-free CS group shows negligible cytotoxicity to 4T1 cells in the concentration range of 0–128 μg/mL. By contrast, the cell viability of 4T1 cells treated with CMS decreased significantly with increasing concentration of CMS, and even the cell viability was only 12 %, at CMS concentration of 128 μg/mL, demonstrating the high therapeutic efficacy of CMS in inducing tumor cell death. Excitingly, CMS has a negligible effect on the proliferation of normal 3T3 fibroblasts (Fig. 3b) at the same concentrations of CMS. Considering that the tumor microenvironment is a complex environment with a lower pH, we further investigated the effect of CMS on 3T3 fibroblasts in an acidic environment. As shown in Fig. S13, CMS also has a negligible effect on the proliferation of 3T3 fibroblasts at pH 6.5 (cell viability >80 %). Besides, the toxicity evaluation of CMS on immune cells DC2.4 (mouse dendritic cell lines) was also performed, and no significant toxicity to DC2.4 was observed after CMS treatment with the concentration ranging from 1 to 128 μg/mL (Fig. S14). These results suggest that CMS has insignificant cytotoxicity to normal cells with good biocompatibility. This tumor-specific eradication of CMS may be due to the higher levels of endogenous H_2O_2 and GSH in tumor cells as

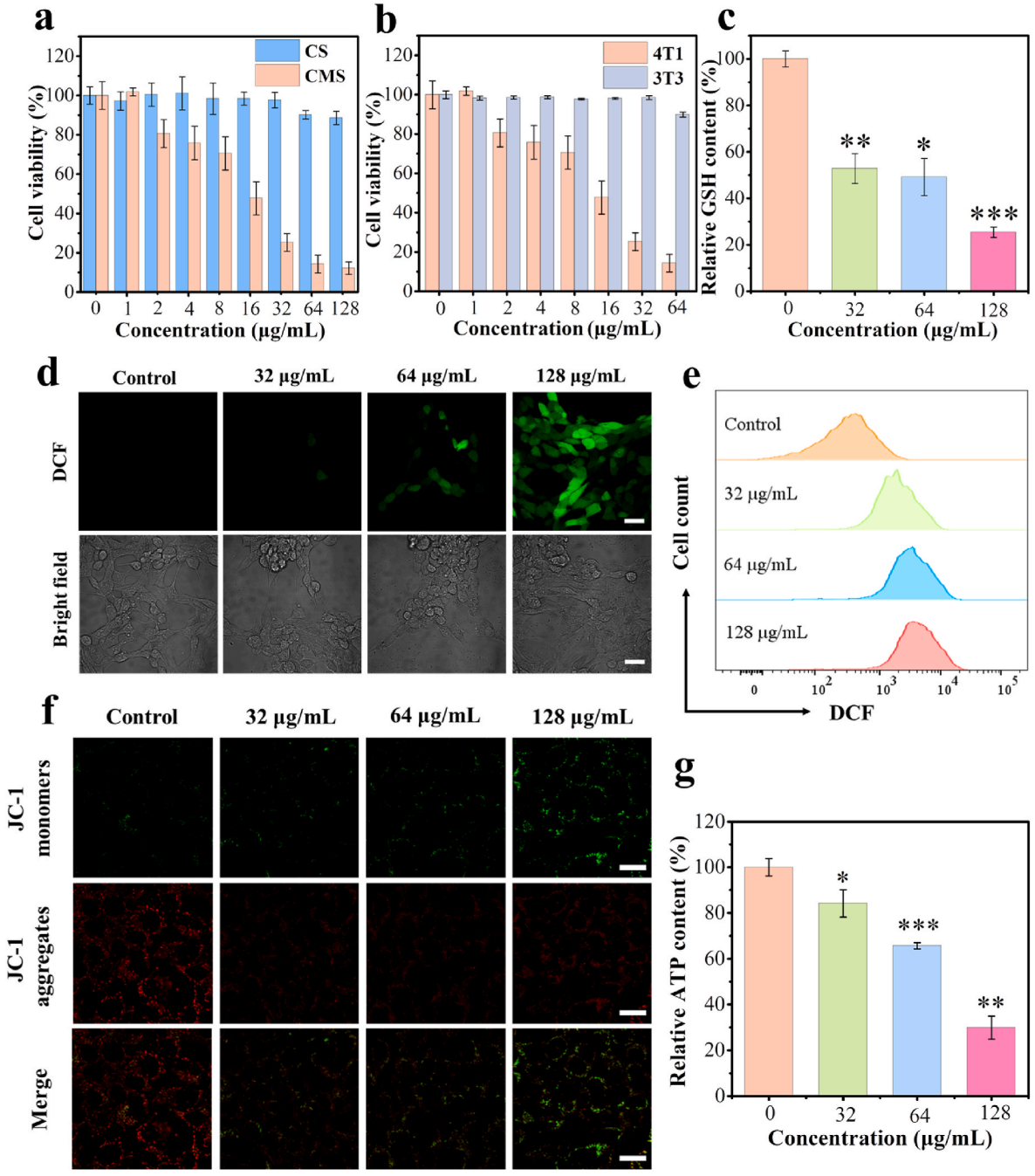

Fig. 3. Evaluations of CMS performance in cellular level. a) Cell viabilities of 4T1 cells after incubation with various concentrations of CMS and CS for 24 h ($n = 5$). b) Cell viabilities of 4T1 cells and 3T3 cells after incubation with various concentrations of CMS for 24 h ($n = 5$). c) Intracellular GSH levels of 4T1 cells after treatment with various concentrations of CMS (32, 64 and 128 μg/mL, $n = 3$). d) CLSM images and e) flow cytometer analysis of DCFH-DA-stained 4T1 cells after treatment with different concentrations of CMS (scale bar = 30 μm). f) CLSM images of 4T1 cells stained with JC-1 after treatment with different concentrations of CMS (scale bar = 20 μm). g) Changes of intracellular ATP contents of 4T1 cells after CMS treatment ($n = 3$). Data represented as mean values ± SD. *, ** and *** represent statistically significant differences at $P < 0.05$, $P < 0.01$ and $P < 0.001$, respectively.

compared to normal cells. Afterward, the cellular uptake of CMS was then evaluated by confocal laser scanning microscopy (CLSM). It is found that FITC-labeled CMS can be effectively internalized by 4T1 cells after 4 h co-incubation (Fig. S15). Based on the CCK8 results, the concentrations of CMS at 32, 64 and 128 μg/mL were selected to evaluate its cellular performance. The inhibitory effect of CMS on tumor cell growth was further confirmed by CLSM and flow cytometry, using Calcein-AM (green)/propidium iodide (PI) (red) kit and Annexin V-FITC/PI kit, respectively (Figs. S16 and 17).

To investigate the antitumor therapeutic mechanism of CMS, the GSH depletion and ROS generation ability of CMS were evaluated *in vitro*. GSH is an abundant endogenous antioxidant that maintains cellular redox homeostasis and inhibits ROS-induced cellular damage. Due to the unique growth and metabolism of tumor cells, the intracellular GSH level is significantly elevated compared to normal cells. Fig. 3c shows the GSH-depleting ability of CMS *in vitro*. It is found that the intracellular GSH levels in the CMS-treated groups decrease significantly with the increase of CMS concentrations. Specifically, the CMS (128 μg/mL) group remains only 25.4 % GSH content of that of the control group, indicating super GSH-depleting ability of CMS, as attributed to the redox reaction of high-valent Mn with GSH.

To characterize the intracellular ROS generation distinctly, 2,7-dichlorofluorescein diacetate (DCFH-DA) was used as the detection probe, as it can be oxidized by ROS to produce 2′,7′-dichlorofluorescein (DCF) with a strong green fluorescence. The CLSM images in Fig. 3d reveal the notably enhanced cellular green fluorescence signals by CMS treatment (Fig. S18), illustrating the robust ROS generation, confirming the ROS generation capability of CMS. Flow cytometry analysis further

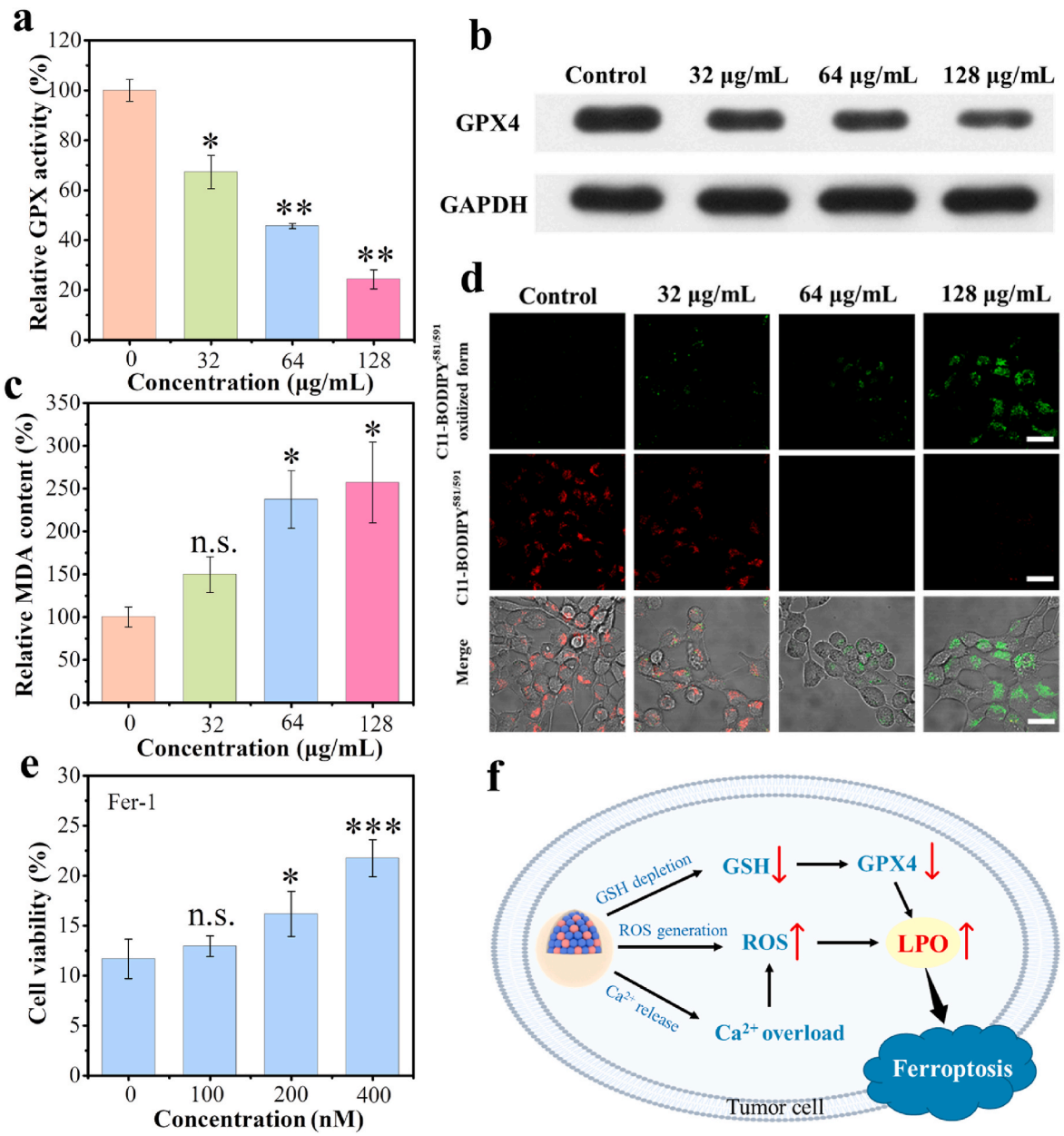

Fig. 4. Intracellular ferroptosis evaluations. a) Relative GPX activities of 4T1 cells after incubation with various concentrations of CMS (32, 64 and 128 μg/mL, $n = 3$), and b) the corresponding Western blotting analysis of GPX4 protein in 4T1 cells after CMS treatment. c) MDA levels of 4T1 cells after CMS treatment ($n = 3$). d) CLSM images of C11-BODIPY$^{581/591}$-stained 4T1 cells after CMS treatment (scale bar = 20 μm). e) The viabilities of 4T1 cells after co-incubation with CMS and varied concentrations of Fer-1 ($n = 3$). f) Schematic diagram of CMS inducing ferroptosis in tumor cells by GSH depletion, ROS generation and Ca^{2+} overload. Data represented as mean values ± SD. *, ** and *** represent statistically significant differences at $P < 0.05$, $P < 0.01$ and $P < 0.001$, respectively.

demonstrated the fluorescence intensity of intracellular ROS, which is in consistent with the CLSM results (Fig. 3e). This increase in intracellular ROS levels after CMS treatment is believed to result from the Mn(II)-catalyzed Fenton-like reaction.

Furthermore, intracellular Ca^{2+} concentrations were studied by CLSM using commercially available Fluo-4 AM as a Ca^{2+} fluorescent probe. As displayed in Fig. S19, the CMS-treated group has an enhanced fluorescence signal as compared to the control group, indicating that the intracellular Ca^{2+} content in 4T1 cells increases after CMS treatment. It is reported that the intracellular Ca^{2+} overload also contributes to the upregulation of intracellular ROS levels [29,30]. In addition, the mitochondrial membrane potential probe JC-1 dye and ATP detection kit were used to assess the changes in mitochondrial membrane potential and intracellular ATP levels. As shown in Fig. 3f, g and Fig. S20, compared with the control group, CMS-treated cells exhibit a significant decrease in mitochondrial membrane potential and intracellular ATP content with increasing concentration of CMS, confirming that CMS can lead to mitochondrial damage, which may be attributed to Ca^{2+} overload and ROS production [28,29]. In brief, as a Ca & Mn dual-ion hybrid nanostimulator, the obtained CMS can increase intracellular ROS levels through Mn(II)-catalyzed Fenton-like reaction and Ca^{2+} overload, facilitating the enhancement of intracellular oxidative stress.

Afterward, the deactivation of GSH-associated GPX was further investigated, and the results showed much decreased activities upon CMS treatments at different concentrations (Fig. 4a). Besides, the results of Western blot analysis further indicated that CMS treatment resulted in down-regulated expression of GPX4 protein (Fig. 4b and Fig. S21). Since the decreased activity of GPX4 could inhibit the toxic LPO to non-toxic hydroxyl compounds, the amount of malondialdehyde (MDA) fragment, as one of the primary LPO end-products of unsaturated lipid, was analyzed. As depicted in Fig. 4c, the MDA amount in the CMS-treated groups increases notably with the increase of CMS concentrations, and that of CMS (128 μg/mL) becomes 2.6 times as large as that in the control group, illustrating the accumulation of LPO for activating ferroptosis. Further, C11-BODIPY$^{581/591}$, an oxidation-sensitive and LPO-specific fluorescent probe, was used to detect the level of LPO in cells. Upon oxidation of C11-BODIPY$^{581/591}$, the maximum emission peak shifts from 590 nm (red) to 510 nm (green) and retains its intrinsic lipophilicity, facilitating the membrane LPO detection. As shown in Fig. 4d and Fig. S22, the red fluorescence decays and the green fluorescence increases with increasing therapeutic CMS dosage, demonstrating the desired CMS-stimulated LPO. Furthermore, the effect of ferrostain-1 (Fer-1, a classical ferroptosis inhibitor) on cell viability in CMS treatment was also examined. As indicated in Fig. 4e, Fer-1 significantly inhibits the decrease in cell viability induced by CMS. Thereinto, the cell viability is increased by 10.1 % with Fer-1 (400 nM), indicating that CMS can trigger ferroptosis of tumor cells. Taken together, the above results indicate that CMS exhibit marked GSH depletion and ROS generation ability, which can obviously enhance the ferroptosis activity by inducing GPX4 inactivation and lead to LPO accumulation (Fig. 4f).

The ROS-ID hypoxia probe (ROS-ID® Hypoxia/Oxidative Stress Detection Kit, Enzo) was further used to access the level of intracellular O_2, as the ROS-ID hypoxia probe can exhibit extremely weak fluorescence under high O_2 concentration. The CLSM images in Fig. S23 show the notably decreased cellular red fluorescence signals by CMS treatment, implying the increase of intracellular O_2 level after CMS treatment due to the CMS catalyzing intracellular H_2O_2 to produce O_2, thereby alleviating the intracellular hypoxia level. Meanwhile, the intracellular H_2O_2 levels in the CMS-treated groups decreased with the increase of CMS concentrations (Fig. S24), ascribed to the decomposition of H_2O_2 by CMS. Besides, the intracellular pH level was detected by using BCECF AM as a pH probe, which is a cell membrane-permeable compound widely used as a fluorescent indicator of intracellular pH. As shown in Fig. S25, a notably increase of cellular green fluorescence signals was observed by CMS treatment, suggesting the increase of intracellular pH level after CMS treatment. The increase of intracellular pH level can be attributed to the H^+ neutralizing ability of carbonate in CMS, which is beneficial to alleviate tumor acidity.

2.4. In vivo evaluation of antitumor performance

Based on the satisfactory therapeutic effect of CMS *in vitro*, the detailed antitumor effect *in vivo* was further investigated. To better study the antitumor mechanism *in vivo*, we chose intratumoral injection which can achieve more drug accumulation in the tumor than that of tail intravenous injection. As depicted in Fig. 5a of the treatment protocol, a bilateral 4T1 tumor model was established. Specifically, Balb/c mice were subcutaneously inoculated with 1×10^6 4T1 cells in the right flank (primary tumor) and then inoculated with 2×10^5 4T1 cells in the left flank (distant tumor). When the primary tumor size reached approximately 80 mm^3, these 4T1-tumor-bearing mice were randomized into four groups. Then, the primary tumors were administered intratumorally with CS (10 mg/kg), CMS (10 mg/kg) or CMS (20 mg/kg) on the 0, 3 and 6 days, while the distal tumors were left untreated. Body weight and tumor volume were recorded every two days for all groups. Tumor-bearing Balb/c mice in all groups showed no unusual changes in body weight during the 14-day treatment process (Fig. 5b), and the histological observation of major organs (heart, liver, spleen, lung and kidney) displayed negligible acute pathological toxicities and adverse effects during the treatment period for the control or treated groups (Fig. S26), suggesting that the treatment in each group had no obvious side effects on the mice. In addition, biochemical analysis of the blood of treated mice shows that the level of detected indexes is consistent with that of the control group (Fig. S27), which further indicates that CMS has negligible toxicity to the liver and kidney with good biological safety. The primary tumor volume changes of different groups during the treatment period are shown in Fig. 5c. Compared with the control group, a limited suppression of tumor growth was observed in the CS group, implying a weak anti-tumor effect. By a sharp contrast, the tumor growth was found to be significantly suppressed in the CMS groups, especially for the CMS (20 mg/kg) group, indicating the excellent antitumor effect of CMS. Moreover, the individual primary tumor growth behaviors of mice in each group feature similar but notably distinguishable tendencies, demonstrating the effective anti-tumor efficacy of CMS (Fig. 5d). After the evaluation process, intact primary tumor resections were obtained and photographed (Fig. 5e), followed by the analysis of primary tumor weights and tumor inhibition rates. As shown in Fig. 5f and Fig. S28, consistent with the result of tumor volume changes, tumor weights in the CMS (20 mg/kg) group were significantly smaller than those in the other groups, with the tumor inhibition rates of 82.7 %, confirming the fulfilling therapeutic effect. Subsequently, H&E-staining, terminal deoxynucleotidyl transferase (TdT) dUTP nick-end labeling (TUNEL) staining and antigen Ki67 immunohistochemical staining of primary tumor tissues were utilized for better understanding the therapeutic efficacy. As displayed in Fig. 5g, compared with other groups, tumor sections in the CMS (20 mg/kg) group exhibited obvious deformation and shrinkage of clenuclei (H&E), remarkably enhanced cell apoptosis (TUNEL) combined with dramatically inhibited cell proliferation (Ki67), which further proved the effective tumor therapeutic effect of CMS.

In addition, the GPX4 deactivation performance of CMS-stimulated ferroptosis was further evaluated *in vivo*. As shown in the immunofluorescence staining of GPX4 in Fig. 5h, compared with control and CS group, obvious decrease in immunofluorescence expression is found in the CMS groups, implying the expression of GPX4 in primary tumor tissues was inhibited by CMS treatment. Besides, obvious decrease of the HIF-1α level in primary tumor tissues after CMS treatment was also found in Fig. 5h, owing to the O_2 generation capability of CMS, since the CMS can efficiently catalyze H_2O_2 to O_2, thus inhibiting the expression of HIF-1α.

More importantly, it is found that the CMS treatment exhibits

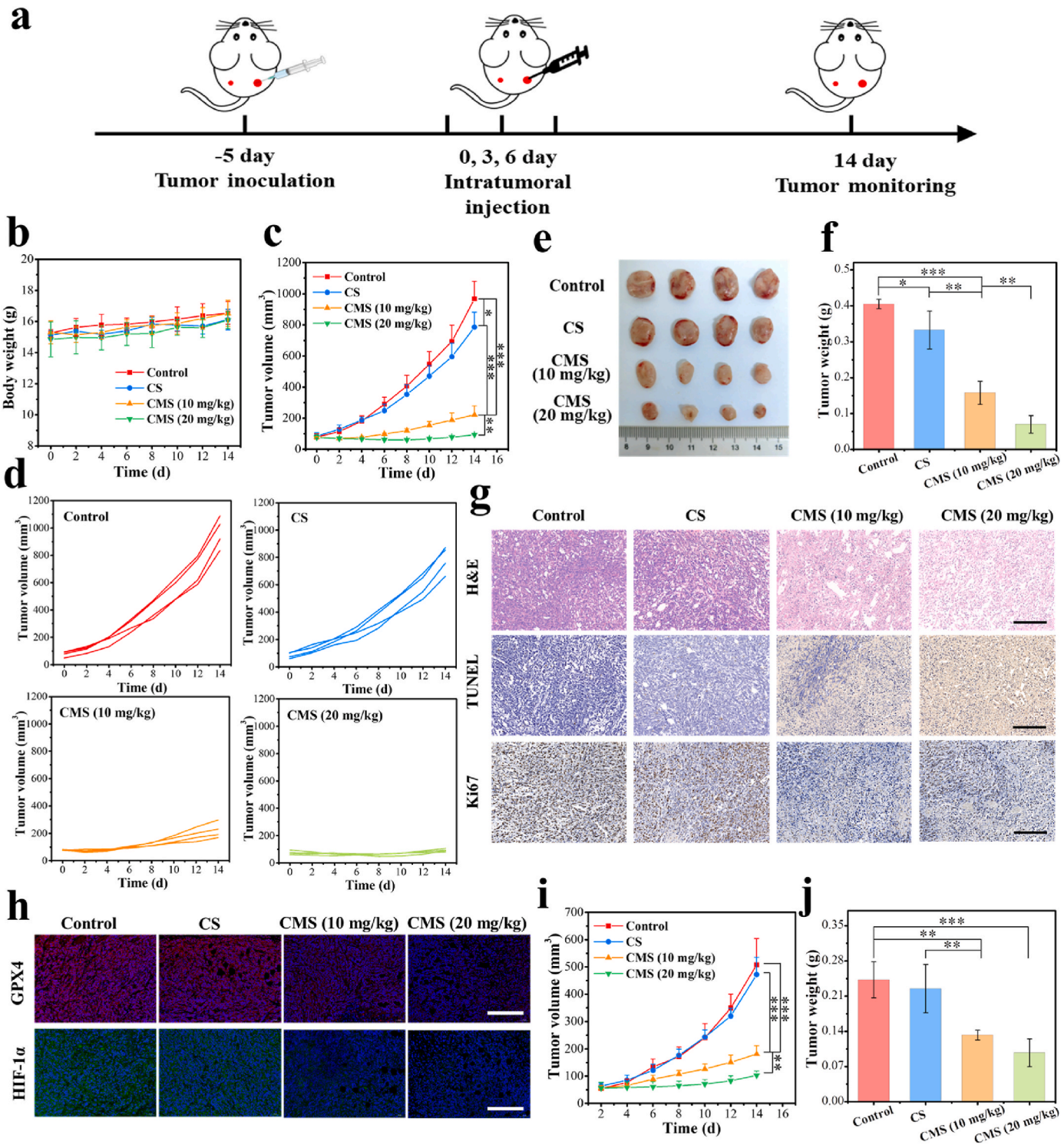

Fig. 5. *In vivo* evaluation of antitumor performance. a) Schematic timeline for *in vivo* therapeutic process using 4T1-tumor-bearing mice. b) Body weight curves of mice during the treatment period. ($n = 4$). c) Time-dependent changes of primary tumor volumes ($n = 4$). d) Growth curve of primary tumor recorded from each mouse in all groups as noted. e) The digital photograph of primary tumor dissections from different groups on Day 14. f) Primary tumor weights of each mouse afterdifferent treatments ($n = 4$). g) H&E, TUNEL and antigen Ki-67 immunohistochemical staining of primary tumor tissues after the above different treatments (scale bar = 200 μm). h) Immunofluorescence staining of GPX4 and HIF-1α in primary tumor tissues after the above different treatments (scale bar = 200 μm). i) Time-dependent changes of distant tumor volumes ($n = 4$). j) Distant tumor weights after different treatments ($n = 4$). Data are represented as mean values ± SD. *, ** and *** represent statistically significant differences at $P < 0.05$, $P < 0.01$ and $P < 0.001$, respectively.

substantial inhibition not only in the primary tumors, but also in the distant tumors. As shown in Fig. 5i and Fig. S29, compared with the control group and CS group, the distant tumor growth of CMS groups was significantly slower. Thereinto, the tumor weights of distant tumor in the CMS (20 mg/kg) group were also significantly smaller than those in the other groups (Fig. 5j and Fig. S30). These results indicate that CMS can also inhibit the growth of distant tumors, which may be attributed to the activation of the anti-tumor immune response.

2.5. In vivo evaluation of anti-tumor immune responses

To reveal the mechanism of anti-tumor immune response by CMS, detailed immunoassay evaluations *in vivo* were further conducted. Fig. 6a shows the schematic timeline for the immunoassay of 4T1-tumor-bearing TNBC models *in vivo*. Macrophages, as one of the main components of innate immunity, involves crucial antitumor characteristics which are essential for cancer immunotherapy. To investigate the macrophage phenotypes in tumors, the tumor tissues were digested into single-cell suspensions and the flow cytometry analysis was performed (Fig. 6b–d and Fig. S31). The quantitative percentage of M2-type macrophages ($F4/80^+CD206^+$) in tumor tissue was 2.5-fold lower in the CMS group than in the control group (Fig. 6b), while the percentage of M1-type macrophages ($F4/80^+CD80^+$) in tumor tissue was 1.9-fold higher in the CMS group than in the control group (Fig. 6c). Overall, the ratio of M1/M2 macrophages in tumor tissue was significantly higher in the CMS group, increasing by 4.8-fold compared to the control group (Fig. S32). These results confirm that the CMS can efficiently polarize M2-type macrophages into M1-type macrophages, mainly ascribed to the O_2-generating capability of CMS. Meanwhile, it is considered that alleviation of tumor hypoxia by CMS is an effective method to modulate the phenotype of TAMs and "awaken" innate immunity.

Furthermore, to investigate the alterations in the tumor immune microenvironment after treatment, we analyzed the tumor tissues 6 h after the last drug administration. By enzyme-linked immunosorbent assay (ELISA), it is found that IFN-β level in tumor tissue is significantly increased after CMS treatment, while no significant change is detected in the CS-treated group (Fig. 6e). More interestingly, the messenger RNA (mRNA) levels of Ifnb1 and Cxcl10, which are induced by STING-dependent signaling or play important roles in the signaling pathway associated with STING and T-cell infiltration in breast tumors, were found to be significantly upregulated in the tumor tissues of the CMS-treated group, but negligibly changed in the CS group by quantitative polymerase chain reaction (qPCR) analysis (Fig. 6f). To better investigate the activation of the STING signaling pathway, its related downstream indicators (p-TBK1, TBK1, p-IRF3 and IRF3) were performed by Western blotting [38,56,57]. As expected, the expression of phosphorylation of two key proteins in the STING pathway, TBK1 (p-TBK1) and IRF3 (p-IRF3), were notably enhanced in the CMS-treated group (Fig. S33). All the above results indicate that due to the incorporation of Mn^{2+}, CMS could activate the STING signaling pathway *in situ* in the tumor, thereby promoting the production and secretion of IFN-I, which could improve the immunosuppressive TME and awaken the innate immune cells.

Considering the ferroptosis induction and innate immunity awakening of CMS together, we further detected the response of immune cells by flow cytometry. The matured DCs ($CD11c^+CD80^+CD86^+$) are implicated as a crucial competent APCs and regulate the adaptive immunity, thus cross-priming effector T cells. To investigate the maturation of DCs, tumor draining lymph nodes were harvested after treatments for flow cytometry analysis (Fig. 6g, h and Fig. S34). Notably, treatment with CMS resulted in the highest percentage of matured DCs, which increased by 2.3-fold compared to the control group, demonstrating that CMS can effectively promote the maturation of DCs for the subsequent adaptive immune response. The activation of anti-tumor immune responses was then further confirmed by measuring the intratumoral infiltration of the CLTs. The fractions of $CD3^+CD8^+$ T cells and $CD3^+CD4^+$ T cells are shown in Fig. 6i, j and Fig. S35. Quantitative analysis indicated that the number of $CD3^+CD8^+$ T cells in the CMS group was much higher than that in the control and CS groups. Meanwhile, the ratio of $CD8^+$ to $CD4^+$ T cells was significantly higher with the CMS treatment, increasing by 3.8-fold compared to that in the control group (Fig. S36). In addition, as shown in Fig. 6k, the levels of various pro-inflammatory cytokines in tumor tissues, including IFN-γ, TNF-α and IL-6, were significantly increased after CMS treatment. These results indicate that the CMS can effectively enhance anti-tumor immunity, promoting the infiltration of CLTs at the tumor site (Fig. 6l).

To further assess the immune-response inducing ability of CMS, the immune cell population in both the distant tumors and spleen was detected by flow cytometry. As shown in Figs. S37 and 38, an obvious $CD8^+$ T cell infiltration was observed in the distant tumors of the CMS group, indicating the activation of anti-tumor immunity. Furthermore, the flow analysis of memory T cells in the spleens of mice exhibited an increase in the relative proportions of the effector memory T cells (T_{EM}, $CD3^+CD8^+CD44^+CD62L^-$) and the central memory T cells (T_{CM}, $CD3^+CD8^+CD44^+CD62L^+$) in the CMS group (Figs. S39 and 40). These results confirm a successful initiation of an immune response and the generation of immune memory after treatment with CMS, contributing to the excellent inhibitory effect of CMS for distant tumor growth. Taken together, all the above results demonstrate that this nanostimulator can be served as an immunoadjuvant, which shows promising potentials in tumor immunotherapy to effectively inhibit tumor recurrence and metastasis of TNBC.

3. Conclusion

In summary, a Ca & Mn dual-ion hybrid nanostimulator was constructed to enhance the anti-tumor immunity of TNBC *via* ferroptosis inducing and innate immunity awakening, which could be served as a ferroptosis inducer and immunoadjuvant for TNBC concurrently. Mn and silica components are integrated onto $CaCO_3$ nanoparticles by cation exchange and heterogeneous nucleation, respectively, to obtain the final Ca & Mn dual-ion hybrid nanomaterial (denoted as CMS). The obtained CMS was found to be beneficial for simultaneous GSH depletion and ROS generation, which was mainly due to the mixed valence state of Mn in CMS. Moreover, as an exotic Ca^{2+} supplier, CMS can boost intracellular Ca^{2+} level, leading to mitochondrial Ca^{2+} overload, further amplifying the oxidative stress. Significantly, the synergy of GSH depletion and ROS bursts further lead to the accumulation of LPO and subsequent ferroptosis in tumor cells. More impressively, CMS can act as an immunoadjuvant to awaken innate immunity by alleviating intratumor hypoxia and Mn^{2+}-induced activation of the STING signaling pathway, which promotes polarization of TAMs from M2 to M1 phenotype and efficient activation of DCs for antigen presentation and subsequent infiltration of tumor-specific CTLs into tumor tissues. Both *in vitro* and *in vivo* results confirm that CMS not only significantly inhibit the growth of primary tumor, but also effectively activate the anti-tumor immunity and inhibit distant tumor growth. Overall, this work highlights an inorganic hybrid nanostimulator to enhance tumor immunogenicity and reverse the immunosuppressive TME by inducing ferroptosis and awakening innate immunity, thereby boosting the anti-tumor immunity, offering a new perspective for effective tumor immunotherapy of TNBC.

4. Experimental section

4.1. Materials

Calcium chloride dihydrate ($CaCl_2{\cdot}2H_2O$), manganese chloride tetrahydrate ($MnCl_2{\cdot}4H_2O$), ammonium carbonate ($(NH_4)_2CO_3$), and methyl blue (MB) were purchased from Sigma-Aldrich. Tetraethyl orthosilicate (TEOS) was purchased from Shanghai Ling Feng Chemical Reagent Co., Ltd. Sodium bicarbonate ($NaHCO_3$), Elliman reagent (DTNB), and reduced glutathione (GSH) were purchased from Shanghai Yien Chemical Reagent Co., Ltd. Hydrogen peroxide (H_2O_2) was purchased from Sinopharm Chemical Reagent Co., Ltd. DMPO was purchased from Japan Tongren Chemical Research Institute. Cell Counting Kit-8 (CCK8) and Annexin V-FITC/PI Apoptosis Detection Kit were purchased from Shanghai Qihai Futai Biotechnology Co., Ltd. Calcein AM/PI Double Stain Kit was purchased from Shanghai Maokang Biotechnology Co., Ltd. DCFH-DA, Fluo-4, JC-1, ATP Assay Kit, GSH

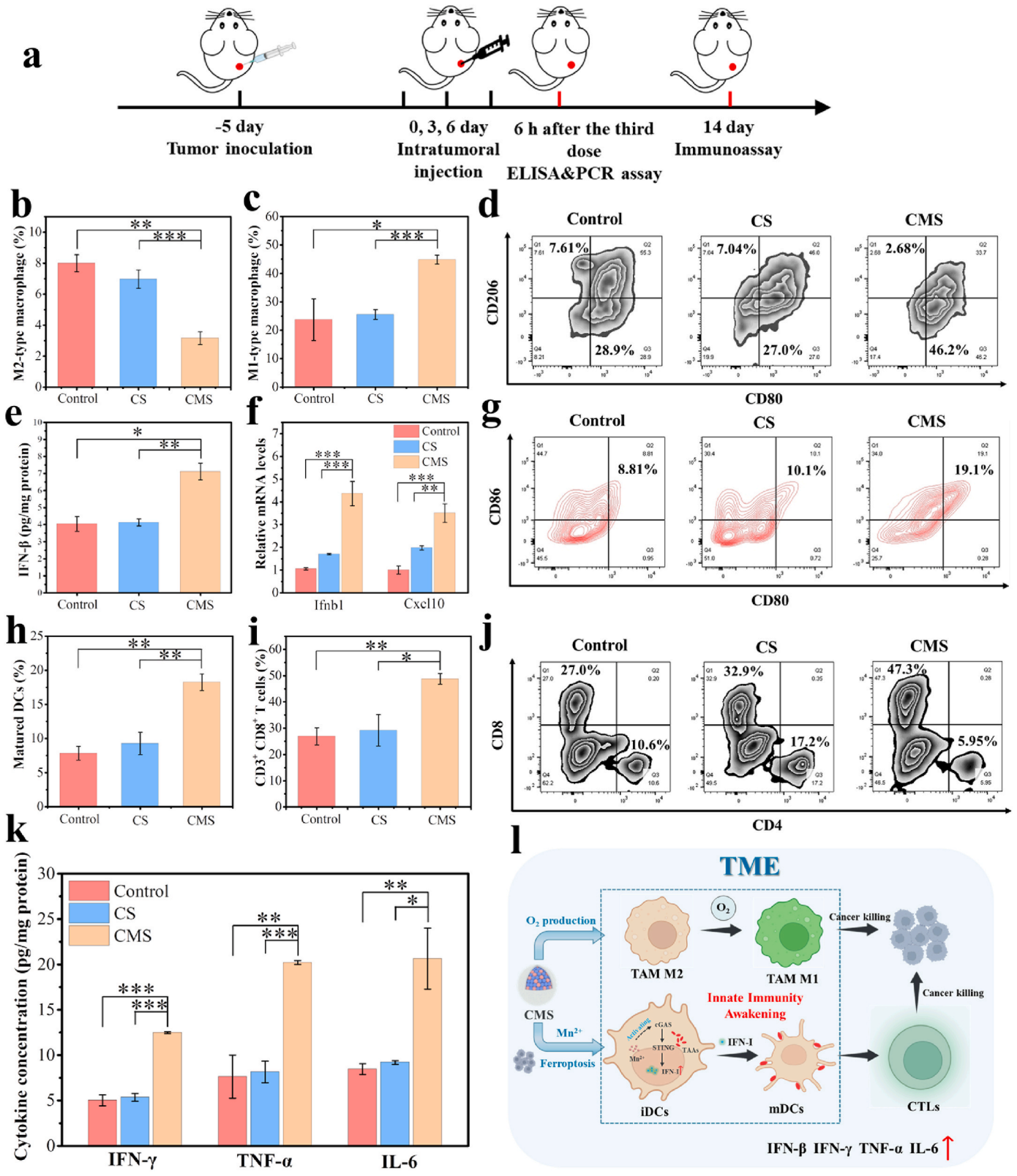

Fig. 6. *In vivo* evaluation of anti-tumor immune responses. a) Schematic timeline for *in vivo* immunoassay of 4T1-tumor-bearing mice. Flow cytometry quantification of b) M2-type macrophages ($F4/80^+CD206^+$) and c) M1-type macrophages ($F4/80^+CD80^+$) in tumor tissues after different treatments. d) Representative flow cytometry plots of TAMs in tumor tissues after different treatments, gated on $F4/80^+$ cells. e) ELISA analysis of the secretion of IFN-β in tumor tissues. f) Quantitative PCR analysis of mRNA levels of Ifnb1 and Cxcl10 in tumor tissues. g) Representative flow cytometry plots and h) quantification of matured DCs ($CD80^+CD86^+$ gated on $CD11c^+$) in lymph nodes of 4T1-tumor-bearing mice after different treatments. i) Flow cytometry quantification of $CD8^+$ T cells and j) representative flow cytometry plots in tumor tissues after different treatments, gated on $CD3^+$ cells. k) ELISA analysis of the secretion of IFN-γ, TNF-α and IL-6 in tumor tissues. l) Schematic diagram of CMS awakening TAMs and DCs to boost anti-tumor immune response. Data represented as mean values ± SD. $n = 3$, *, ** and *** represent statistically significant differences at $P < 0.05$, $P < 0.01$ and $P < 0.001$, respectively.

Assay Kit, Lipid Peroxidation MDA Assay Kit, and BCA Protein Assay Kit were purchased from Beyotime Biotechnology. Glutathione Peroxidase (GPx) Assay Kit was purchased from Regen Biotechnology. Ferrostain-1 (Fer-1) was purchased from MedChemExpress. C11-BODIPY$^{581/591}$ was purchased from GLPBIO. GPX4 Monoclonal antibody was purchased from Proteintech. APC/CY7 anti-mouse CD45, PE anti-mouse CD3, FITC anti-mouse CD8, PerCP/CY5.5 anti-mouse CD4, PE/CY7 anti-mouse CD11b, BV421 anti-mouse F4/80, AF647 anti-mouse CD206, BV650 anti-mouse CD80, Percp-cy5.5 anti-mouse CD45, BV421 anti-mouse CD80, PE anti-mouse CD86, and PE-CY7 anti-mouse CD11c were purchased from Shanghai Universal Biotech.

4.2. Characterizations

Transmission electron microscope (TEM) images and element mapping were obtained on a JEM-2100F electron microscope with an operating voltage of 200 kV. Scanning electron microscope (SEM) image was obtained on a Zeiss Gemini 450 electron microscope. XPS analysis was conducted on a Thermo ESCALAB 250Xi X-ray photoelectron spectrometer. Hydrodynamic diameter and ζ-potential of materials were measured on a Zetasizer Nanoseries (Nano ZS90). UV–vis absorption spectra were obtained on a UV-2600 spectrometer. Element content was determined by inductively coupled plasma optical emission spectrometry (ICP-OES, Agilent 725). ESR spectra were acquired on an electron spin resonance paramagnetic wave spectrometer (JEOL-FA200). Dissolved oxygen concentration was completed on JPBJ-610L portable dissolved oxygen meter. Confocal laser scanning microscopy (CLSM) images were obtained on FV1000 system (Olympus Company). Quantitative analysis of cell apoptosis and immune cells were performed on a flow cytometer (BD LSRFortessa).

4.3. Synthesis of CMS

$CaCO_3$ nanoparticles were synthesized via the gas diffusion method [58]. Then, CM and CMS nanoparticles were synthesized via a modified method based on our previous work [49], in which the final Mn/Ca molar ratio was controlled to be approximately 0.5. In brief, 40 mg of $CaCO_3$ nanoparticles dispersed in 40 mL of ethanol, then 20 mL of $MnCl_2$ ethanol solution (1 mol/L) was added into this dispersion and stirred for 24 h at 25 °C. The final product (CM nanoparticles) was collected by centrifugation and washed with ethanol, then redispersed in ethanol for further use. For the synthesis of CMS nanoparticles: 3.4 mL of ammonium solution was added into 75 mL of CM nanoparticles ethanol dispersion and stirred for 1 h at 25 °C. Then, 20 μL of TEOS was added to the above mixture and string for another 24 h. The final product (CMS nanoparticles) was collected by centrifugation and washed with ethanol, then redispersed in ethanol for further use.

4.4. Ca and Mn release of CMS

CMS was dissolved in PBS buffer at 5.5, 6.5 and 7.4. At different time points (10, 30, 60, 120, 240 and 360 min), the supernatants were collected by centrifugation. The release of Ca and Mn was determined by ICP-OES.

4.5. Hemolytic analysis of CMS

1.5 mL of fresh blood collected from 2 five-week-old female Balb/c mice was transferred to EDTA k2 anticoagulant tubes. The supernatant was removed by centrifugation at 2000 rpm for 10 min. After several washes with saline, 200 μL of the suspension was added to 2 mL of saline containing 0.016, 0.031, 0.062, 0.125, 0.25, 0.5 and 1 mg/mL CMS. Ultrapure water and saline were used as positive and negative controls, respectively. After 2 h of incubation, an image was taken after centrifugation (2000 rpm, 10 min), the supernatant was measured for absorbance at 540 nm. Hemolysis rate of red blood cell was then calculated.

$$\text{Hemolysis rate (\%)} = (OD_{sample}\text{-}OD_{saline})/(OD_{water}\text{-}OD_{saline}) \times 100\ \%$$

4.6. GSH depletion capacity of CMS

The GSH amount was detected by DTNB at the absorbance of 412 nm. CMS (200 μg/mL) was con-incubated with GSH (0.5 mM) for 4 h. Then DTNB (0.5 mM) was added to detect the residual GSH, and H_2O_2 (3 mM) as a GSH depletion inducer was also evaluated. The time (0.5, 1, 2, 4, 6 and 12 h)-dependent GSH depletion was also determined.

4.7. Fenton-like-mediated ·OH production of CMS

·OH was detected through UV–vis absorption spectroscopy and ESR spectroscopy. For UV–vis method, MB was used as the detection probe. In detail, MB (10 μg/mL), $NaHCO_3$ (25 mM), H_2O_2 (10 mM), and CMS (100 μg/mL) were mixed and reacted for 30 min. The MB degradation was detected by the characteristic absorption change at 664 nm. For the ESR assay, DMPO was used as the ·OH trapping agent. Typically, CMS (100 μg/mL), $NaHCO_3$ (25 mM), H_2O_2 (200 μM), and DMPO were mixed. Then, the mixture was transferred into a quartz capillary for measurement on the ESR spectrometer.

4.8. O_2 generation performance of CMS

Oxygen (O_2) generation of CMS was evaluated by dissolved oxygen analyzer (JPBJ-610L). Specifically, CMS was dispersed in 5 mL water with the concentration of 100 μg/mL, followed by the addition of H_2O_2 with the concentration of 1 mM. Then, the O_2 production was recorded by the instrument. Afterward, various concentrations of H_2O_2 (1, 0.5, 0.25 and 0.125 mM) with CMS (100 μg/mL) were further evaluated the O_2 generation.

4.9. Cellular culture

Mammary carcinoma cell lines (4T1), normal fibroblast cell lines (3T3) and mouse dendritic cell lines (DC2.4) were obtained from National Collection of Authenticated Cell Cultures. The cells were incubated with RPMI 1640 medium, including 10 % FBS, 0.5 % penicillin, and 0.5 % streptomycin under humidified condition with 5 % CO_2 at 37 °C.

4.10. Cell viability assay

The 4T1 cells were seeded in 96-well plates (8×10^3 cells per well). After culture for 24 h, medium was replaced by fresh complete RPMI 1640 medium containing CMS or CS at difference concentration (0, 1, 2, 4, 8, 16, 32, 64 and 128 μg/mL). After further incubation for 24 h, cells were washed by PBS for twice, and then the cell viability was measured by CCK8 assay. To verify the biocompatibility of CMS, 3T3 cells and DC2.4 cells were incubated with CMS for 24 h, and other procedures are the as above. For the killing mechanism study of CMS to 4T1 cells, 4T1 cells were con-incubated with CMS (64 μg/mL) and Fer-1 (0, 100, 200 and 400 nM) for 24 h, and the cell viability was measured by CCK8 assay.

4.11. Cell uptake of CMS

Confocal laser scanning microscopy (CLSM) was employed to analyze cell uptake of CMS. 4T1 cells were seeded on 35 mm CLSM-specific dishes (2×10^5 cells per dish). After culture for 24 h, medium was replaced by fresh RPMI 1640 medium with FITC-labeled CMS (128 μg/mL). After incubation for 0, 1 and 4 h, cells were washed with PBS and observed by CLSM.

4.12. Cell apoptosis analysis

CLSM and flow cytometer were employed to analyze cell apoptosis. For CLSM observation, 4T1 cells were seeded on 35 mm CLSM-specific dishes (2×10^5 cells per dish). After culture for 24 h, medium was replaced by fresh RPMI 1640 medium with CMS (32, 64 and 128 μg/mL). After incubation for 18 h, dishes were washed with PBS and then Calcein AM/PI dye was used to stain cells for CLSM observation. For flow cytometer analysis, procedures were similar to the above except that cells were cultured in 6-well plates and incubated with CMS for 8 h. At the end of co-incubation, cells were treated with Annexin V-FITC/PI dye for flow cytometer analysis.

4.13. Intracellular ROS and LPO measurement

4T1 cells were planted in 35 mm CLSM-specific dishes (2×10^5 cells per dish) and incubated overnight. Then, the cells were incubated with CMS (32, 64 and 128 μg/mL) for 4 h. Subsequently, the culture medium was replaced by fresh DCFH-DA-containing medium (10 μM) for 30 min, followed by washing with PBS buffer. Finally, the ROS fluorescence was observed by CLSM. For flow cytometer analysis of intracellular ROS levels, procedures were similar to the above except that cells were cultured in 6-well plates. For LPO assay, procedures were similar to the above except that cells were incubated with CMS for 6 h and stained by C11-BODIPY$^{581/591}$ probe for 30 min. Finally, the fluorescence was observed by CLSM.

4.14. Intracellular GSH, GPX, and MDA assay

The 4T1 cells were seeded in 6-well plates (2×10^5 cells per well) and incubated overnight. Then cells were co-incubated with CMS (32, 64 and 128 μg/mL) for 6 h. The intracellular GSH amount was evaluated using GSH Assay Kit; the GPX activity was measured using Glutathione Peroxidase (GPX) Assay Kit; and the MDA amount was monitored using Lipid Peroxidation MDA Assay Kit. In addition, the protein concentration of cellular sample was assayed using BCA Protein Assay Kit.

4.15. Western blot analysis of intracellular GPX4 expression

The 4T1 cells were seeded in 6-well plates (2×10^5 cells per well) and incubated for 24 h. Then cells were co-incubated with CMS (32, 64 and 128 μg/mL) for 10 h. Subsequently, GPX4 antibody was applied to stained the collected cells, and GPX4 expression levels were detected using electrophoresis.

4.16. Evaluation of accumulation of intracellular Ca^{2+} and changes of intracellular mitochondrial membrane potential and ATP content

For intracellular Ca^{2+} measurement, 4T1 cells were planted in 35 mm CLSM-specific dishes (2×10^5 cells per dish) and incubated overnight. Then, the cells were incubated with CMS (32, 64 and 128 μg/mL) for 4 h. Subsequently, the cells were washed with PBS and stained with Fluo-4 AM. Finally, the stained cells were imaged using CLSM. For intracellular mitochondrial membrane potential assay, procedures were similar to the above except that cells were incubated with CMS for 18 h and stained by JC-1 probe. For intracellular ATP content measurement, 4T1 cells were seeded in 6-well plates (2×10^5 cells per well) and incubated for 24 h. Then, the cells were incubated with CMS (32, 64 and 128 μg/mL) for 24 h. Finally, the ATP content was measured using ATP Assay Kit.

4.17. Intracellular O_2 assay, intracellular H_2O_2 measurement and intracellular pH detection

The ROS-ID hypoxia probe (ROS-ID® Hypoxia/Oxidative Stress Detection Kit, Enzo) was used to assay the intracellular O_2 level. The cells were incubated with CMS (32, 64 and 128 μg/mL) for 6 h. Subsequently, the cells were washed with PBS and stained with hypoxia probe. Finally, the stained cells were imaged using CLSM. For intracellular H_2O_2 measurement, the cells were incubated with CMS (32, 64 and 128 μg/mL) for 6 h, and the intracellular H_2O_2 level was evaluated using Hydrogen Peroxide (H_2O_2) Content. For the detection of intracellular pH, BCECF AM was used as a pH probe. The cells were incubated with CMS (32, 64 and 128 μg/mL) for 24 h. Afterward, the cells were washed with PBS and then stained with BCECF AM. The stained cells were imaged using CLSM.

4.18. Animal models

All animal experiments were approved by the Animal Center of Tongji University, and conducted following the Guide for Care and Use of Laboratory Animals (TJLAC-020-228).

4.19. In vivo antitumor efficacy

To establish a bilateral tumor model, female Balb/c mice (5 weeks) were subcutaneously inoculated with 4T1 cells ($\approx 1 \times 10^6$ cells) in the right flank (primary tumor) and then inoculated with 4T1 cells ($\approx 2 \times 10^5$ cells) in the left flank (distant tumor). The growth of tumors was monitored daily. Tumor volume was calculated using the equation: $V = (ab^2)/2$, where a represents the length of the tumor and b represents the width of the tumor. Then, 4T1-bearing Balb/c mice were randomly divided into four groups ($n = 4$) and treated with intratumoral injection for the primary tumor and no treatment for the distant tumor. Considering the therapeutic efficacy and pain reduction in mice, we chose to administer three intratumoral injections once every 3 days to replenish the drug concentration at the tumor site and to avoid infection and leakage at the injection site. Group I received no treatment (control). Group II received intratumoral CS (10 mg/kg) on day 0, day 3 and day 6. Group III received intratumorally CMS (10 mg/kg) on day 0, day 3 and day 6. Group IV received CMS (20 mg/kg) intratumorally on day 0, day 3 and day 6. Tumor volume and body weight were recorded every 2 days for 14 days. After 14 days, all mice were sacrificed, and tumors were harvested for photography and weight recording, and one mouse from each group was randomly selected for H&E staining of major organs (heart, liver, spleen, lung, kidney). In addition, 24 h after the last treatment, one mouse from each group was randomly selected and its primary tumors were harvested for H&E sections, antigen Ki-67, TUNEL, GPX4, and HIF-1α assays.

4.20. In vivo immune activation analysis

4T1 cells ($\approx 1 \times 10^6$ cells) in 100 μL PBS were subcutaneously injected into the right flank of the Balb/c mice (female, 5 weeks). 4T1-bearing Balb/c mice with tumor volume of 80 mm^3 were randomly divided into three groups ($n = 3$). Group I received no treatment (control). Group II received intratumoral CS (10 mg/kg) on day 0, day 3 and day 6. Group III received CMS (10 mg/kg) intratumorally on day 0, day 3 and day 6. Then, 6 h after the last treatment, the mice were euthanized and the tumors were harvested to determine the cytokines release of IFN-β, IL-6, IFN-γ and TNF-α, the expression of Ifnb1 and Cxcl10 mRNA, and the protein expression of p-TBK1, TBK1, p-IRF3 and IRF3. In addition, 8 days after the last treatment, the mice were euthanized and the tumors and lymph nodes were collected and digested into single cell suspension in PBS solution, which were further measured by flow cytometry.

The tumor single cells were stained with fluorophore conjugated anti-CD45, anti-CD11b, anti-F4/80, anti-CD206, anti-CD80, anti-CD3, anti-CD4 and anti-CD8 and further measured by flow cytometry to demonstrate the expression of tumor associated macrophages (TAMs) and the existence of T cells. Moreover, the lymph single cells were

stained with fluorophore conjugated anti-CD45, anti-CD11c, anti-CD80 and anti-CD86 to illustrate dendritic cells (DCs) by flow cytometry.

For the immunoassays of the distant tumors and spleens, a bilateral tumor model was established. Female Balb/c mice (5 weeks) were subcutaneously inoculated with 4T1 cells (≈1 × 10^6 cells) in the right flank (primary tumor) and then inoculated with 4T1 cells (≈2 × 10^5 cells) in the left flank (distant tumor). Bilateral 4T1-bearing Balb/c mice with primary tumor volume of 80 mm^3 were randomly divided into three groups ($n = 3$) and treated with intratumoral injection for the primary tumor and no treatment for the distant tumor. Group I received no treatment (control). Group II received intratumoral CS (10 mg/kg) on day 0, day 3 and day 6. Group III received CMS (10 mg/kg) intratumorally on day 0, day 3 and day 6. Finally, the mice were euthanized and the distant tumors and spleens were collected and digested into single cell suspension in PBS solution, which were further measured by flow cytometry. The distant tumor single cells were stained with fluorophore conjugated anti-CD45, anti-CD3, anti-CD4 anti-CD8 and further measured by flow cytometry to demonstrate the existence of T cells. Moreover, the spleen single cells were stained with fluorophore conjugated anti-CD3, anti-CD8, anti-CD44 and anti-CD62L to illustrate memory T cells by flow cytometry.

4.21. Statistical analysis

The significant difference of experimental data was evaluated through one-way analysis of variance (ANOVA). The calculated probability (P) was distinguished between $^*P$ values < 0.05, $^{**}P$ values < 0.01 and $^{***}P$ values < 0.001. Date was taken as mean ± standard error.

Ethics approval

All the animal experiments were performed with the approval of the Tongji University Experimental Animal Center and all procedures were performed according to the guidelines and animal welfare protocols. The animal biomedical research authorization number is TJLAC-020-228.

CRediT authorship contribution statement

Xi Deng: Conceptualization, Data curation, Investigation, Writing – original draft. **Tianzhi Liu:** Conceptualization, Funding acquisition, Writing – review & editing. **Yutong Zhu:** Data curation, Methodology. **Jufeng Chen:** Methodology. **Ze Song:** Methodology. **Zhangpeng Shi:** Methodology. **Hangrong Chen:** Funding acquisition, Supervision, Writing – review & editing.

Declaration of competing interest

The authors declare that they have no known competing financial interests or personal relationships that could have appeared to influence the work reported in this paper.

Acknowledgements

This work was supported by the National Key Research and Development Program of China (Grant No. 2021YFB3801000), the National Natural Science Foundation of China (Grant No. 32030061), the Basic Research Program of Shanghai Municipal Government (Grant No. 21JC1406000), the Shanghai Sailing Program (Grant No. 21YF1454200), and Shanghai International Cooperation Project (Grant No. 23490712900). All the animal experiments were performed with the approval of the Tongji University Experimental Animal Center, and the animal biomedical research authorization number is TJLAC-020-228.

Appendix A. Supplementary data

Supplementary data to this article can be found online at https://doi.org/10.1016/j.bioactmat.2023.11.017.

References

[1] C. Luo, P. Wang, S. He, J. Zhu, Y. Shi, J. Wang, Progress and prospect of immunotherapy for triple-negative breast cancer, Front. Oncol. 12 (2022), 919072, https://doi.org/10.3389/fonc.2022.919072.
[2] R.A. Leon-Ferre, M.P. Goetz, Advances in systemic therapies for triple negative breast cancer, BMJ 381 (2023), e071674, https://doi.org/10.1136/bmj-2022-071674.
[3] P. Chowdhury, U. Ghosh, K. Samanta, M. Jaggi, S.C. Chauhan, M.M. Yallapu, Bioactive nanotherapeutic trends to combat triple negative breast cancer, Bioact. Mater. 6 (2021) 3269–3287, https://doi.org/10.1016/j.bioactmat.2021.02.037.
[4] I. Mellman, G. Coukos, G. Dranoff, Cancer immunotherapy comes of age, Nature 480 (2011) 480–489, https://doi.org/10.1038/nature10673.
[5] S. Adams, M.E. Gatti-Mays, K. Kalinsky, L.A. Korde, E. Sharon, L. Amiri-Kordestani, H. Bear, H.L. McArthur, E. Frank, J. Perlmutter, D.B. Page, B. Vincent, J.F. Hayes, J.L. Gulley, J.K. Litton, G.N. Hortobagyi, S. Chia, I. Krop, J. White, J. Sparano, M. L. Disis, E.A. Mittendorf, Current landscape of immunotherapy in breast cancer: a review, JAMA Oncol. 5 (2019) 1205–1214, https://doi.org/10.1001/jamaoncol.2018.7147.
[6] C. Jiang, X. Li, F. Pan, L. Zhang, H. Yu, J. Zhang, J. Zou, T. Zhong, D. Zhang, Y. Yang, Y. Li, P. Zhang, Ferroptosis and pyroptosis Co-activated nanomodulator for "cold" tumor immunotherapy and lung metastasis inhibition, Adv. Funct. Mater. 33 (2023), 2211698, https://doi.org/10.1002/adfm.202211698.
[7] H. Zhong, G. Chen, T. Li, J. Huang, M. Lin, B. Li, Z. Xiao, X. Shuai, Nanodrug augmenting antitumor immunity for enhanced TNBC therapy via pyroptosis and cGAS-STING activation, Nano Lett. 23 (2023) 5083, https://doi.org/10.1021/acs.nanolett.3c01008.
[8] K.G.K. Deepak, R. Vempati, G.P. Nagaraju, V.R. Dasari, N. S, D.N. Rao, R.R. Malla, Tumor microenvironment: challenges and opportunities in targeting metastasis of triple negative breast cancer, Pharmacol. Res. 153 (2020), 104683, https://doi.org/10.1016/j.phrs.2020.104683.
[9] Y. Xu, J. Xiong, X. Sun, H. Gao, Targeted nanomedicines remodeling immunosuppressive tumor microenvironment for enhanced cancer immunotherapy, Acta Pharm. Sin. B 12 (2022) 4327–4347, https://doi.org/10.1016/j.apsb.2022.11.001.
[10] M.L. Guevara, F. Persano, S. Persano, Nano-immunotherapy: overcoming tumour immune evasion, Semin, Cancer Biol. 69 (2021) 238–248, https://doi.org/10.1016/j.semcancer.2019.11.010.
[11] L. Zeng, S. Ding, Y. Cao, C. Li, B. Zhao, Z. Ma, J. Zhou, Y. Hu, X. Zhang, Y. Yang, G. Duan, X.-w. Bian, G. Tian, A MOF-based potent ferroptosis inducer for enhanced radiotherapy of triple negative breast cancer, ACS Nano 17 (2023), 13195, https://doi.org/10.1021/acsnano.3c00048.
[12] D. Wang, G. Qiu, X. Zhu, Q. Wang, C. Zhu, C. Fang, J. Liu, K. Zhang, Y. Liu, Macrophage-inherited exosome excise tumor immunosuppression to expedite immune-activated ferroptosis, J. Immunother. Cancer 11 (2023), e006516, https://doi.org/10.1136/jitc-2022-006516.
[13] X. Yao, W. Li, D. Fang, C. Xiao, X. Wu, M. Li, Z. Luo, Emerging roles of energy metabolism in ferroptosis regulation of tumor cells, Adv. Sci. 8 (2021), 2100997, https://doi.org/10.1002/advs.202100997.
[14] L. Yao, M.-M. Zhao, Q.-W. Luo, Y.-C. Zhang, T.-T. Liu, Z. Yang, M. Liao, P. Tu, K.-W. Zeng, Carbon quantum dots-based nanozyme from coffee induces cancer cell ferroptosis to activate antitumor immunity, ACS Nano 16 (2022) 9228–9239, https://doi.org/10.1021/acsnano.2c01619.
[15] K. Li, C. Lin, M. Li, K. Xu, Y. He, Y. Mao, L. Lu, W. Geng, X. Li, Z. Luo, K. Cai, Multienzyme-like reactivity cooperatively impairs glutathione peroxidase 4 and ferroptosis suppressor protein 1 pathways in triple-negative breast cancer for sensitized ferroptosis therapy, ACS Nano 16 (2022) 2381–2398, https://doi.org/10.1021/acsnano.1c08664.
[16] J. Cheng, L. Li, D. Jin, Y. Dai, Y. Zhu, J. Zou, M. Liu, W. Yu, J. Yu, Y. Sun, X. Chen, Y. Liu, Boosting ferroptosis therapy with iridium single-atom nanocatalyst in ultralow metal content, Adv. Mater. 35 (2023), 2210037, https://doi.org/10.1002/adma.202210037.
[17] Y. Du, R. Zhang, J. Yang, S. Liu, J. Zhou, R. Zhao, F. He, Y. Zhang, P. Yang, J. Lin, A "closed-loop" therapeutic strategy based on mutually reinforced ferroptosis and immunotherapy, Adv. Funct. Mater. 32 (2022), 2111784, https://doi.org/10.1002/adfm.202111784.
[18] Z. Zhou, H. Liang, R. Yang, Y. Yang, J. Dong, Y. Di, M. Sun, Glutathione depletion-induced activation of dimersomes for potentiating the ferroptosis and immunotherapy of "cold" tumor, Angew. Chem. Int. Ed. 61 (2022), e202202843, https://doi.org/10.1002/anie.202202843.
[19] J. Zhang, Y. Qin, Z. Wang, W. Zhang, S. Liu, W. Wei, X. Wang, J. Zhao, Ferroptosis-inducing inorganic arsenic(II) sulfide nanocrystals enhance immune activation, Nano Res. 16 (2023) 9760, https://doi.org/10.1007/s12274-023-5617-y.
[20] L. Zhao, X. Zhou, F. Xie, L. Zhang, H. Yan, J. Huang, C. Zhang, F. Zhou, J. Chen, L. Zhang, Ferroptosis in cancer and cancer immunotherapy, Cancer Commun. 42 (2022) 88–116, https://doi.org/10.1002/cac2.12250.
[21] J. Du, M. Zhou, Q. Chen, Y. Tao, J. Ren, Y. Zhang, H. Qin, Disrupting intracellular iron homeostasis by engineered metal-organic framework for nanocatalytic tumor

therapy in synergy with autophagy amplification-promoted ferroptosis, Adv. Funct. Mater. 33 (2023), 2215244, https://doi.org/10.1002/adfm.202215244.
[22] X. Chen, R. Kang, G. Kroemer, D. Tang, Broadening horizons: the role of ferroptosis in cancer, Nat. Rev. Clin. Oncol. 18 (2021) 280–296, https://doi.org/10.1038/s41571-020-00462-0.
[23] C. Wu, Z. Liu, Z. Chen, D. Xu, L. Chen, H. Lin, J. Shi, A nonferrous ferroptosis-like strategy for antioxidant inhibition–synergized nanocatalytic tumor therapeutics, Adv. Sci. 7 (2021), eabj8833, https://doi.org/10.1126/sciadv.abj8833.
[24] Q. Wang, F. Shaik, X. Lu, W. Zhang, Y. Wu, H. Qian, W. Zhang, Amorphous NiB@IrOx nanozymes trigger efficient apoptosis-ferroptosis hybrid therapy, Acta Biomater. 155 (2023) 575–587, https://doi.org/10.1016/j.actbio.2022.10.048.
[25] P. Zhu, Y. Pu, M. Wang, W. Wu, H. Qin, J. Shi, MnOOH-catalyzed autoxidation of glutathione for reactive oxygen species production and nanocatalytic tumor innate immunotherapy, J. Am. Chem. Soc. 145 (2023) 5803–5815, https://doi.org/10.1021/jacs.2c12942.
[26] F. Wu, Y. Du, J. Yang, B. Shao, Z. Mi, Y. Yao, Y. Cui, F. He, Y. Zhang, P. Yang, Peroxidase-like active nanomedicine with dual glutathione depletion property to restore oxaliplatin chemosensitivity and promote programmed cell death, ACS Nano 16 (2022) 3647–3663, https://doi.org/10.1021/acsnano.1c06777.
[27] F. Fu, W. Wang, L. Wu, W. Wang, Z. Huang, Y. Huang, C. Wu, X. Pan, Inhalable biomineralized liposomes for cyclic Ca2+-burst-centered endoplasmic reticulum stress enhanced lung cancer ferroptosis therapy, ACS Nano 17 (2023) 5486–5502, https://doi.org/10.1021/acsnano.2c10830.
[28] Y. Li, S. Zhou, H. Song, T. Yu, X. Zheng, Q. Chu, CaCO3 nanoparticles incorporated with KAE to enable amplified calcium overload cancer therapy, Biomaterials 277 (2021), 121080, https://doi.org/10.1016/j.biomaterials.2021.121080.
[29] P. Zheng, B. Ding, Z. Jiang, W. Xu, G. Li, J. Ding, X. Chen, Ultrasound-augmented mitochondrial calcium ion overload by calcium nanomodulator to induce immunogenic cell death, Nano Lett. 21 (2021) 2088–2093, https://doi.org/10.1021/acs.nanolett.0c04778.
[30] M. Zhang, R. Song, Y. Liu, Z. Yi, X. Meng, J. Zhang, Z. Tang, Z. Yao, Y. Liu, X. Liu, W. Bu, Calcium-overload-mediated tumor therapy by calcium peroxide nanoparticles, Chem 5 (2019) 2171–2182, https://doi.org/10.1016/j.chempr.2019.06.003.
[31] D. Wang, M. Zhang, Y. Zhang, G. Qiu, J. Chen, X. Zhu, C. Kong, X. Lu, X. Liang, L. Duan, C. Fang, J. Liu, K. Zhang, T. Luo, Intraparticle double-scattering-decoded sonogenetics for augmenting immune checkpoint blockade and CAR-T therapy, Adv. Sci. 9 (2022), 2203106, https://doi.org/10.1002/advs.202203106.
[32] D. Wang, M. Zhang, G. Qiu, C. Rong, X. Zhu, G. Qin, C. Kong, J. Zhou, X. Liang, Z. Bu, J. Liu, T. Luo, J. Yang, K. Zhang, Extracellular matrix viscosity reprogramming by in situ Au bioreactor-boosted microwavegenetics disables tumor escape in CAR-T immunotherapy, ACS Nano 17 (2023) 5503–5516, https://doi.org/10.1021/acsnano.2c10845.
[33] E. Kvedaraite, F. Ginhoux, Human dendritic cells in cancer, Sci. Immunol. 7 (2022), eabm9409, https://doi.org/10.1126/sciimmunol.abm9409.
[34] Y. Liu, L. Wang, Q. Song, M. Ali, W.N. Crowe, G.L. Kucera, G.A. Hawkins, S. Soker, K.W. Thomas, L.D. Miller, Y. Lu, C.R. Bellinger, W. Zhang, A.A. Habib, W.J. Petty, D. Zhao, Intrapleural nano-immunotherapy promotes innate and adaptive immune responses to enhance anti-PD-L1 therapy for malignant pleural effusion, Nat. Nanotechnol. 17 (2022) 206–216, https://doi.org/10.1038/s41565-021-01032-w.
[35] H. Guo, J. Huang, Y. Tan, W. Wu, T. Huang, N. Zhang, S. Chen, C. Zhang, X. Xie, X. Shuai, M. Xu, Nanodrug shows spatiotemporally controlled release of anti-PD-L1 antibody and STING agonist to effectively inhibit tumor progression after radiofrequency ablation, Nano Today 43 (2022), 101425, https://doi.org/10.1016/j.nantod.2022.101425.
[36] M. Luo, H. Wang, Z. Wang, H. Cai, Z. Lu, Y. Li, M. Du, G. Huang, C. Wang, X. Chen, M.R. Porembka, J. Lea, A.E. Frankel, Y.-X. Fu, Z.J. Chen, J. Gao, A STING-activating nanovaccine for cancer immunotherapy, Nat. Nanotechnol. 12 (2017) 648–654, https://doi.org/10.1038/nnano.2017.52.
[37] C. Wang, Y. Guan, M. Lv, R. Zhang, Z. Guo, X. Wei, X. Du, J. Yang, T. Li, Y. Wan, X. Su, X. Huang, Z. Jiang, Manganese increases the sensitivity of the cGAS-STING pathway for double-stranded DNA and is required for the host defense against DNA viruses, Immunity 48 (2018) 675–687, https://doi.org/10.1016/j.immuni.2018.03.017.
[38] X. Sun, Y. Zhang, J. Li, K.S. Park, K. Han, X. Zhou, Y. Xu, J. Nam, J. Xu, X. Shi, L. Wei, Y.L. Lei, J.J. Moon, Amplifying STING activation by cyclic dinucleotide–manganese particles for local and systemic cancer metalloimmunotherapy, Nat. Nanotechnol. 16 (2021) 1260–1270, https://doi.org/10.1038/s41565-021-00962-9.
[39] Y. Zhao, Y. Pan, K. Zou, Z. Lan, G. Cheng, Q. Mai, H. Cui, Q. Meng, T. Chen, L. Rao, L. Ma, G. Yu, Biomimetic manganese-based theranostic nanoplatform for cancer multimodal imaging and twofold immunotherapy, Bioact. Mater. 19 (2023) 237–250, https://doi.org/10.1016/j.bioactmat.2022.04.011.
[40] J.-L. Liang, X.-K. Jin, S.-M. Zhang, Q.-X. Huang, P. Ji, X.-C. Deng, S.-X. Cheng, W.-H. Chen, X.-Z. Zhang, Specific activation of cGAS-STING pathway by nanotherapeutics-mediated ferroptosis evoked endogenous signaling for boosting systemic tumor immunotherapy, Sci. Bull. 68 (2023) 622–636, https://doi.org/10.1016/j.scib.2023.02.027.
[41] I. Vitale, G. Manic, L.M. Coussens, G. Kroemer, L. Galluzzi, Macrophages and metabolism in the tumor microenvironment, Cell Metabol. 30 (2019) 36–50, https://doi.org/10.1016/j.cmet.2019.06.001.
[42] Z. Chen, F. Han, Y. Du, H. Shi, W. Zhou, Hypoxic microenvironment in cancer: molecular mechanisms and therapeutic interventions, Signal Transduct. Targeted Ther. 8 (2023) 70, https://doi.org/10.1038/s41392-023-01332-8.
[43] M. Song, T. Liu, C. Shi, X. Zhang, X. Chen, Bioconjugated manganese dioxide nanoparticles enhance chemotherapy response by priming tumor-associated macrophages toward M1-like phenotype and attenuating tumor hypoxia, ACS Nano 10 (2016) 633–647, https://doi.org/10.1021/acsnano.5b06779.
[44] Z. Yang, Y. Luo, H. Yu, K. Liang, M. Wang, Q. Wang, B. Yin, H. Chen, Reshaping the tumor immune microenvironment based on a light-activated nanoplatform for efficient cancer therapy, Adv. Mater. 34 (2022), 2108908, https://doi.org/10.1002/adma.202108908.
[45] Z. Dai, Q. Zhang, X. Li, Q. Chen, J. Chen, M. Wang, H. Chen, In situ forming pH/ROS-responsive niche-like hydrogel for ultrasound-mediated multiple therapy in synergy with potentiating anti-tumor immunity, Mater. Today 65 (2023) 62–77, https://doi.org/10.1016/j.mattod.2023.03.025.
[46] Y. Wang, J. Yu, Z. Luo, Q. Shi, G. Liu, F. Wu, Z. Wang, Y. Huang, D. Zhou, Engineering endogenous tumor-associated macrophage-targeted biomimetic nano-RBC to reprogram tumor immunosuppressive microenvironment for enhanced chemo-immunotherapy, Adv. Mater. 33 (2021), 2103497, https://doi.org/10.1002/adma.202103497.
[47] J. Huang, X. Leng, T. Jiang, L. Xu, J. Zheng, M. Fang, J. Wang, Z. Wang, L. Zhang, Oxygen-carrying nanoplatform to reprogram tumor immunosuppressive microenvironment and enhance photothermal-immunotherapy, Mater, Today Bio 19 (2023), 100555, https://doi.org/10.1016/j.mtbio.2023.100555.
[48] Y. Liu, D. Xu, Y. Liu, X. Zheng, J. Zang, W. Ye, Y. Zhao, R. He, S. Ruan, T. Zhang, H. Dong, Y. Li, Y. Li, Remotely boosting hyaluronidase activity to normalize the hypoxic immunosuppressive tumor microenvironment for photothermal immunotherapy, Biomaterials 284 (2022), 121516, https://doi.org/10.1016/j.biomaterials.2022.121516.
[49] T. Liu, Q. Wan, Y. Luo, M. Chen, C. Zou, M. Ma, X. Liu, H. Chen, On-demand detaching nanosystem for the spatiotemporal control of cancer theranostics, ACS Appl. Mater. Interfaces 11 (2019) 16285–16295, https://doi.org/10.1021/acsami.9b02062.
[50] V.P. Santos, O.S.G.P. Soares, J.J.W. Bakker, M.F.R. Pereira, J.J.M. Órfão, J. Gascon, F. Kapteijn, J.L. Figueiredo, Structural and chemical disorder of cryptomelane promoted by alkali doping: influence on catalytic properties, J. Catal. 293 (2012) 165–174, https://doi.org/10.1016/j.jcat.2012.06.020.
[51] K. Liang, H. Sun, Z. Yang, H. Yu, J. Shen, X. Wang, H. Chen, Breaking the redox homeostasis: an albumin-based multifunctional nanoagent for GSH depletion-assisted chemo-/chemodynamic combination therapy, Adv. Funct. Mater. 31 (2021), 2100355, https://doi.org/10.1002/adfm.202100355.
[52] S.I. Liochev, I. Fridovich, Carbon dioxide mediates Mn(II)-catalyzed decomposition of hydrogen peroxide and peroxidation reactions, Proc. Natl. Acad. Sci. USA 101 (2004) 12485–12490, https://doi.org/10.1073/pnas.0404911101.
[53] L.-S. Lin, J. Song, L. Song, K. Ke, Y. Liu, Z. Zhou, Z. Shen, J. Li, Z. Yang, W. Tang, G. Niu, H.-H. Yang, X. Chen, Simultaneous fenton-like ion delivery and glutathione depletion by MnO2-based nanoagent to enhance chemodynamic therapy, Angew. Chem. Int. Ed. 57 (2018) 4902–4906, https://doi.org/10.1002/anie.201712027.
[54] Z. Sun, Z. Wang, T. Wang, J. Wang, H. Zhang, Z. Li, S. Wang, F. Sheng, J. Yu, Y. Hou, Biodegradable MnO-based nanoparticles with engineering surface for tumor therapy: simultaneous fenton-like ion delivery and immune activation, ACS Nano 16 (2022) 11862–11875, https://doi.org/10.1021/acsnano.2c00969.
[55] Y. Feng, Y. Liu, X. Ma, L. Xu, D. Ding, L. Chen, Z. Wang, R. Qin, W. Sun, H. Chen, Intracellular marriage of bicarbonate and Mn ions as “immune ion reactors” to regulate redox homeostasis and enhanced antitumor immune responses, J. Nanobiotechnol. 20 (2022) 193, https://doi.org/10.1186/s12951-022-01404-x.
[56] W. Song, S.-J. Song, J. Kuang, H. Yang, T. Yu, F. Yang, T. Wan, Y. Xu, S.-T. Wei, M.-X. Li, Y. Xiong, Y. Zhou, W.-X. Qiu, Activating innate immunity by a STING signal amplifier for local and systemic immunotherapy, ACS Nano 16 (2022) 15977–15993, https://doi.org/10.1021/acsnano.2c03509.
[57] Q. Luo, Z. Duan, X. Li, L. Gu, L. Ren, H. Zhu, X. Tian, R. Chen, H. Zhang, Q. Gong, Z. Gu, K. Luo, Branched polymer-based redox/enzyme-activatable photodynamic nanoagent to trigger STING-dependent immune responses for enhanced therapeutic effect, Adv. Funct. Mater. 32 (2022), 2110408, https://doi.org/10.1002/adfm.202110408.
[58] S.-F. Chen, H. Cölfen, M. Antonietti, S.-H. Yu, Ethanol assisted synthesis of pure and stable amorphous calcium carbonate nanoparticles, Chem. Commun. 49 (2013) 9564–9566, https://doi.org/10.1039/C3CC45427D.